Master Thesis

Imaging of the Earth's Plasmasphere in the Extreme Ultraviolet

極端紫外光による地球プラズマ圏の撮像

Go Murakami

Space and Planetary Science Group

Department of Earth & Planetary Science

Graduate School of Science, The University of Tokyo

February 28, 2008

Abstract

The Earth's plasmasphere is the region where dense plasma originated from the ionosphere is captured along the closed geomagnetic field lines. Intensive observations using spacecrafts revealed the dynamical aspect of the plasmasphere changing depending on geomagnetic conditions. The cycles of erosion and refilling of the plasma population in the plasmasphere have been studied extensively in the past. However, conventional *in-situ* measurements are local observations with which it is difficult to separate the temporal development and the spatial structure of the plasmasphere. To overcome this difficulty, the visualization of the plasmasphere has recently been emphasized. Helium ions are the second major component in the plasmasphere (almost 10% of the total amount), and resonantly scatter the solar EUV emission at 30.4 nm. For this reason, detecting this emission leads us to the global imaging of the plasmasphere.

Recent advances in satellite-based imaging techniques have made it possible to routinely obtain full global images of the plasmasphere. The Extreme Ultraviolet Imager (EUV) on the IMAGE satellite gave us complete sequential pictures. I statistically examined the plasmapause response to the southward turning of the interplanetary magnetic field (IMF) using sequential EUV images of the plasmasphere. By tracking the location of the plasmapause in sequential EUV images, I calculated the plasmapause radial velocity and then estimated the time development of the convection electric field at the plasmapause. Consequently, my research indicates that the plasmapause response to the southward turning of the IMF takes 10-30 min, with an average of 18 min. This timescale suggests that the convection electric field propagates from the magnetopause to the inner magnetosphere through the ionosphere.

In the near future, the Telescope of Extreme Ultraviolet (TEX) mounted in the Upper atmosphere and Plasma Imager (UPI) on the SELENE satellite will provide global images of near-Earth plasmas from the lunar orbit. The SELENE satellite was launched and sent to the Moon in 2007. The UPI-TEX imager detects the resonance scattering emissions of helium ions (He II: 30.4 nm) and oxygen ions (O II: 83.4 nm) to take images of the plasmasphere and the polar wind, respectively. I calibrated the performance of the UPI-TEX imager before the launch. As a result, the UPI-TEX has a total sensitivity of 0.014 cps/Rayleigh/bin for the He II (30.4 nm) and 0.0036 cps/Rayleigh/bin for the O II (83.4 nm). Imaging of the plasmasphere with the 2-min

exposure and the 0.09-R_E resolution improves our understanding of the distribution of plasma in the inner magnetosphere and the forces that control it. On the other hand, the remote sensing at O II with the 30-min exposure and the 0.5-R_E resolution gives the first global image of the polar wind and make significant contributions to our understanding of the transport routes and mechanisms of the cold O^+ ions.

Furthermore, I have developed a high-resolution imaging detector with five microchannel plates (MCPs) in a set of V- and Z-stacks and a resistive anode encoder (RAE) for the future missions. In a position-sensitive system with an RAE, the spatial resolution depends on the signal-to-noise ratios at the anode terminals. Therefore, a high and stable electron gain of MCPs allows the position determination of each photoelectron event with a high spatial resolution. I investigated the effect of the negative inter-stack potential on the PHD and the spatial resolution by means of calculation and experiments. As a result, applying the negative inter-stack potential reduced the width of the PHD and improved the spatial resolution to 400×400 pixels. The results enable us to optimize and apply the technique to the future missions.

要旨

地球近傍にはプラズマ圏と呼ばれる高密度の冷たいプラズマで満たされた領域が存在する．地球近傍におけるプラズマの運動を支配するのは主に地球の自転が引き起こす共回転電場と太陽風が磁気圏内に引き起こす大規模な対流電場である．これらを重ね合わせた電場におけるプラズマの $E\times B$ ドリフトの運動からプラズマ圏の形成を説明できる．太陽風の変動に応じてプラズマ圏の構造が活発に変化することが過去の人工衛星による直接観測から明らかにされた．しかし直接観測では衛星のその場の情報しか得られないため，プラズマ圏の時間変化と空間変化を分離することは困難であった．こうした問題を解決するため，プラズマの可視化により地球近傍でのプラズマの振る舞いを大局的に把握しようとする試みがなされてきた．プラズマ圏を構成する主なイオンのうちヘリウムイオンと酸素イオンは波長 30.4 nm と 83.4 nm においてそれぞれ共鳴散乱を起こすため，これらの光を捉えることでプラズマ圏全体の時間変動を明らかにすることができる．

2000 年に打ち上げられた IMAGE 衛星搭載の極端紫外光撮像器（EUV）はヘリウムイオンからの共鳴散乱光を連続的に撮像し，プラズマ圏の構造や運動を明らかにした．私は2000－2001 年にEUV 撮像器が捉えた画像を用いて太陽風の変動に対するプラズマ圏の応答を統計的に調べた．その結果，太陽風の変動に応じてプラズマ圏が運動するまでに10－30 分，平均18 分の遅れがあることを明らかにした．この結果は太陽風電場が磁気圏前面から電離圏を経由して夜側内部磁気圏へと伝播することを示唆している．

また 2007 年に打ち上げられた月周回衛星 SELENE（かぐや）では極端紫外光望遠鏡（UPI-TEX）によるヘリウムイオン（30.4 nm）および酸素イオン（83.4 nm）の撮像が計画されている．この観測では月周回軌道からの撮像であるため常にプラズマ圏全体を視野内に収めることができデータ数の向上が見込まれる．さらに人工衛星による酸素イオンの撮像は世界初の試みであり，極域から流出するプラズマの経路の同定に大きな貢献が期待される．私は UPI-TEX 撮像器の地上較正試験を行い，波長 30.4 nm において 0.014 cps/Rayleigh/bin，波長 83.4 nm において 0.0036 cps/Rayleigh/bin の感度をもつことを確認した．UPI-TEX 撮像器は時間分解能 2 分および空間分解能 0.09 R_{E} でプラズマ圏のヘリウムイオンを，また時間分解能 30 分および空間分解能 0.5 R_{E} で極域から流出する酸素イオンをそれぞれ撮像でき，科学目標を十分達成できる．

太陽風の早い変動とプラズマ圏の運動をより高精度で比較するには, プラズマポーズのわずかな変動を捉えられる高い位置分解能をもつ検出器が必要となる. そこで私は将来のプラズマ圏撮像計画に向け, 2 段と 3 段を組み合わせたマイクロチャンネルプレート（MCP）とレジスティブアノードを用いた検出器を開発した. 私はシミュレーションおよび実験を行い検出器の性能を評価した. その結果, 2 段と 3 段の MCP の間に逆向きに電圧を印加することで波高分布の幅を狭め, 位置分解能を UPI-TEX 撮像器に比べ約 3 倍に向上できることを確認した.

Contents

1 General Introduction

1.1 The Earth's Plasmasphere

The magnetosphere is a region around the Earth in which the Earth's magnetic field is the dominant influence and controls the motions of charged particles. Figure 1.1 shows the results of a synthesis of *in-situ* and ground-based observations over 40 years and represents today's generally accepted global view of the Earth's magnetosphere. In the inner magnetosphere, the magnetic field configuration is dipolar like with perturbation at its outer edge caused by the external pressure change of the solar wind. At ionospheric altitude below 1000km in the mid and high latitude, the dipole field is nearly vertical. The charged particles in the ionosphere are free to move upward along magnetic field lines and populate the higher-altitude regions of the Earth's magnetosphere. The charged particles, which are predominantly electrons and protons with energies not exceeding several electron volts [eV], form a region of cold dense plasma (shown in Figure 1.1) and is called the plasmasphere.

The existence of a sharp outer boundary of the plasmasphere, corresponding to the plasmapause, was first discovered in the early 1960s [*Carpenter*, 1963]. Analysis of whistler waves recorded at ground stations established the plasmapause as a permanent feature within the magnetosphere. After the establishment of the definition of the plasmasphere, satellite *in-situ* measurements were used to investigate the inner magnetosphere, particularly the plasmasphere in the 1970s. Figure 1.2 shows the dominance of H^+, He^+, and O^+ measured by a mass spectrometer onboard the OGO 5 satellite, showing density profiles plotted versus the *L*-shell parameter (the distance of the equatorial crossing point of the field line from the Earth's center, measured in Earth's radii). The density profile of He^+ is very similar in shape to that of H^+. The density distribution of those ions sharply decreases by a factor of 100 or more. In Figure 1.2, the position of the outer boundary, the plasmapause, at L=4.9 is evident in both H^+ and He^+. The outer plasmasphere consists of about 90% H^+ and about 10% He^+ with only a trace of O^+.

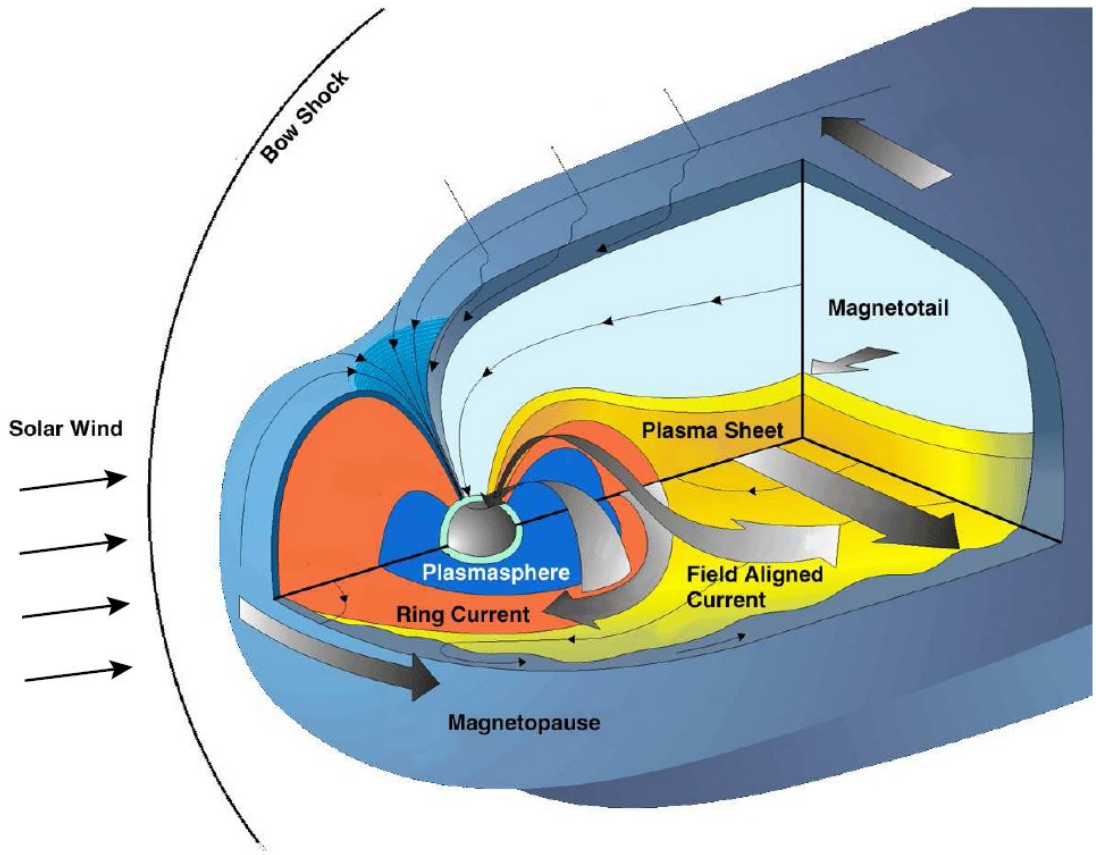

Figure 1.1: A schematic diagram of a generally accepted global representation of the Earth's magnetosphere. This picture has been synthesized from a vast number of localized observations made over the past four decades throughout many of the regions [*Williams et al.*, 1992].

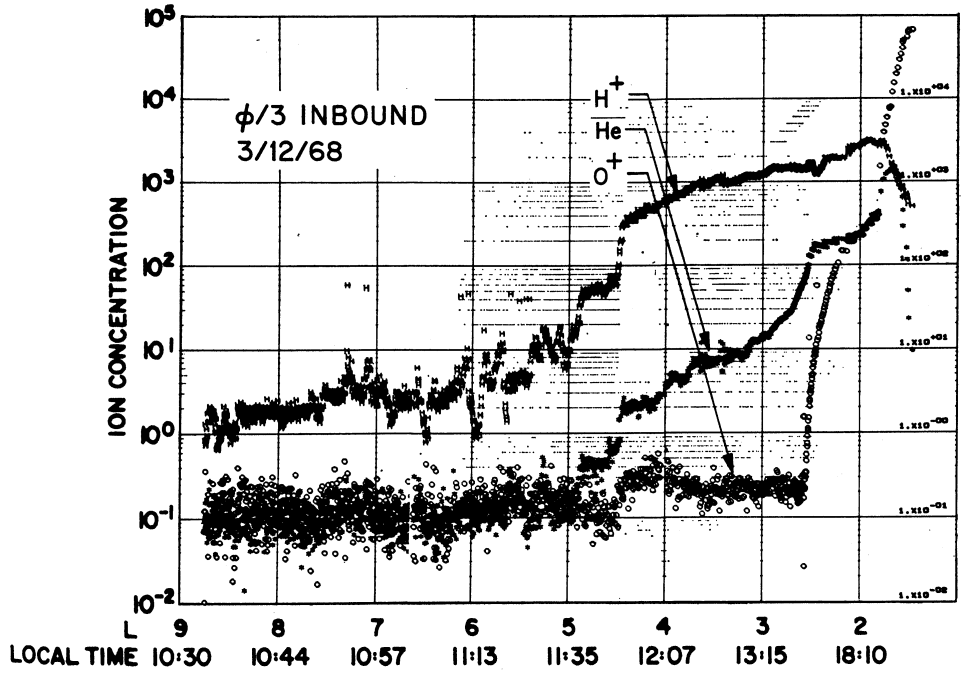

Figure 1.2: A typical inbound plasmapause crossing observed by OGO 5 showing the H^+, He^+, and O^+ ion concentrations as a function of L and local time [*Chappell et al.*, 1970].

On the other hand, there have been theoretical approaches for the comprehension of the plasmasphere [*Nishida*, 1966]. *Nishida* [1966] represented a clear explanation of the formation of the plasmapause. There is a large-scale electric field directed from dawn to dusk. This electric field originated from the solar wind magnetic field and penetrates into the magnetosphere. The plasma in the magnetosphere drifts to $E \times B$ direction due to this electric field (E is the convection electric field, and B is the Earth's magnetic field). When the corotation with the Earth is superposed on a large-scale convection, a convection profile shown in Figure 1.3 is obtained. The motions of cold plasmas, such as those in the plasmasphere, are explained by the $E \times B$ drift convection, since their gradient and curvature drifts are very small. In Figure 1.3, it can be seen that the streamlines of the plasma convections can be categorized into two distinctly different flow regimes by a separatrix between open and closed drift paths: those which pass through the magnetosphere, and those which circulate around the Earth. The latter closed region inside the separatrix continues to be filled up to high densities with ionospheric plasmas. Outside this separatrix, cold plasmas on an open drift trajectory generally drift sunward from the tail, and flux tubes are filled up to

relatively lower densities of cold plasmas due to their shorter lifetimes in the magnetosphere. As a result, the separatrix can be recognized as the outer boundary of dense plasma, i.e., the plasmapause.

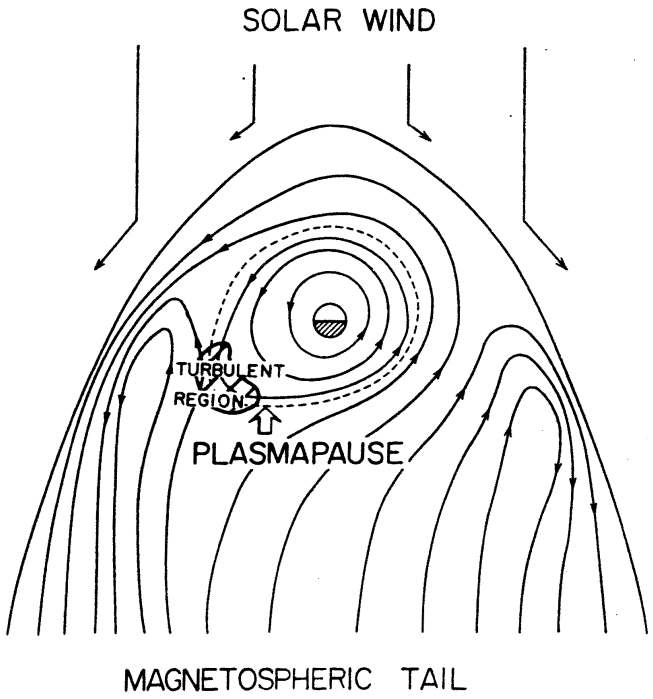

Figure 1.3: Streamlines of the magnetospheric plasma motion obtained by superposing the motion due to the Earth's rotation on the flow of the solar-wind-induced convection. The boundary between two groups of streamlines, i.e., those that pass the tail and those that do not, is suggested to be the plasmapause (dotted curve). The region of turbulence is also indicated [*Nishida*, 1966].

Intensive observation using spacecraft followed and revealed the dynamical aspect of the plasmasphere changing depending on geomagnetic conditions. It became clear that the plasmapause position is closely correlated with average magnetic activity over a 2 to 6-hour period, e.g., the K_p index [*Chappell*, 1970]. The plasmasphere shrinks with increasing the magnetic activity in a very well-behaved, predictable manner. This variation in the radius of the plasmasphere depending on the magnetic activity is shown in Figure 1.4. This figure represents the superposed results over more than 40 passes of the satellite. The decrease in the radius of the plasmapause is accompanied by an

increased steepness in the density gradient at the plasmapause, while the total concentration levels inside and outside the plasmapause remain approximately ~10^3 ions/cm^3 and ~1 ions/cm^3, respectively.

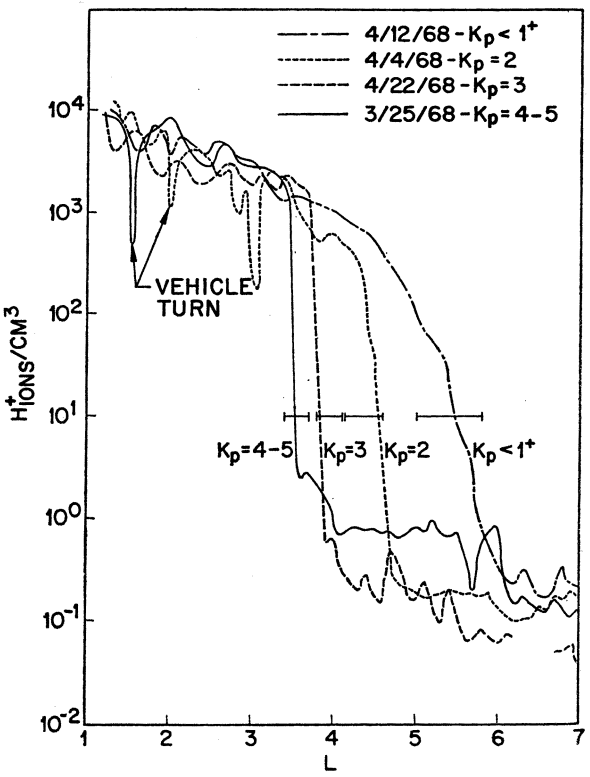

Figure 1.4: A composite graph of H^+ concentration measured by OGO 5 showing the reaction of the plasmasphere in the nightside region to changes in the level of magnetic activity. The plasmapause is found to be steep and move to lower L values with increasing activity [*Chappell et al.*, 1970].

When the southward IMF encounters the Earth's northward magnetic field at the dayside magnetopause, it leads to the process of magnetic field line merging or reconnection, driving sunward convection in the inner magnetosphere [*Dungey*, 1961]. Figure 1.5 shows a schematic diagram of the plasma motion in the enhanced convection electric field. The enhanced convection electric field triggered by a southward turning of the IMF forms new $E \times B$ drift trajectories, and particles that were previously on the outermost closed trajectories suddenly find themselves on open trajectories and drift toward the dayside magnetopause. Thus, the outer layers of the plasmasphere are stripped away and the plasmasphere shrinks.

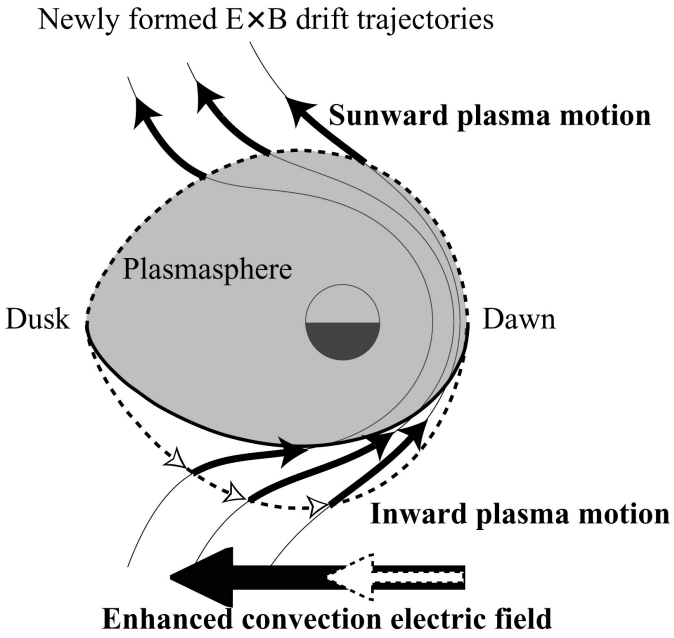

Figure 1.5: A schematic diagram of the plasma motion in the convection electric field enhanced by the southward turning of the IMF. The dashed line indicates the previously formed plasmapause. After the enhancement, the nightside plasmapause on the previous plasmapause move inward as black arrows along the newly formed $E \times B$ drift trajectories. The dayside plasma moves sunward and the structure called as the dayside bulge or plume forms.

1.2 Imaging the Plasmasphere

In-situ measurements along the spacecraft's path were intensively performed in the early 1970s, and revealed dynamic aspects of the plasmasphere. However, the *in-situ* measurements are local observations with which it is difficult to separate the temporal development and the spatial structure of the plasmasphere. To overcome this difficulty, various efforts have sought to understand the global distribution of the plasmasphere by visualization.

Helium and oxygen ions are the second and third major components in the plasmasphere, as shown in Figure 1.2, and resonantly scatter the solar extreme ultraviolet (EUV) emission at 30.4 nm (He II) and 83.4 nm (O II), respectively. For this reason, detecting these emissions leads us to the global imaging of the plasmasphere. The fundamental technology to detect the EUV emission began with the He II emission

(30.4 nm), which was first detected on a sounding rocket experiment [*Johnson et al.*, 1971]. After this discovery, proof-of-concept observations to give inside-out views of the plasmasphere have been performed by both sounding rockets (e.g. *Ogawa and Tohmatsu*, 1971; *Paresce et al.*, 1974; *Yoshikawa et al.*, 1997) and the spacecraft (e.g. *Weller and Meier*, 1974: *Chakrabarti et al.*, 1982; *Meier et al.*, 1998). However, it is difficult to extract the geophysical information on the outer plasmasphere from its inside.

The two-dimensional He II imaging of the Earth's plasmasphere from its outside was first done by the Planet-B (Nozomi) spacecraft [*Nakamura et al.*, 2000]. *Yoshikawa et al.* [2000a, 200b, 2001] first presented static EUV images of the plasmasphere and the inner magnetosphere. Figure 1.6 represents the 2-D image observed by the XUV scanner onboard the Planet-B spacecraft. The image shows the plasmasphere shape averaged over the noon-duskside sector. The dipole magnetic field lines of L = 4 and 5 are also shown. While the inner magnetic field line corresponds to the plasmapause, the outer magnetic field line corresponds to the outer boundary of the dusk bulge [*Yoshikawa et al.*, 2000a].

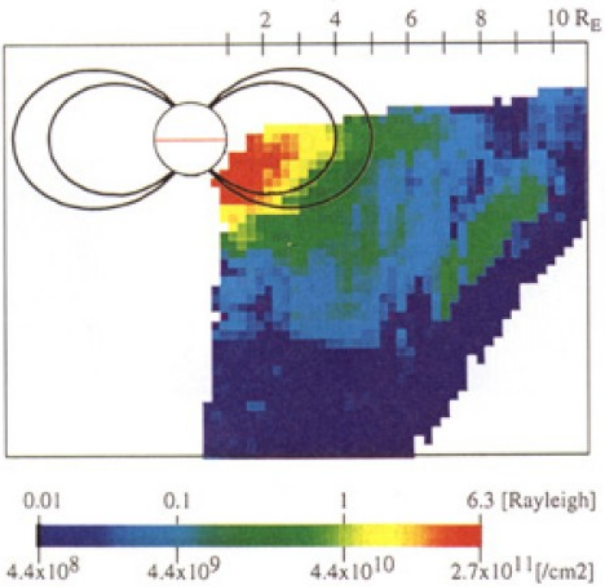

Figure 1.6: Two-dimensional imagery assuming the symmetrical shape of the plasmasphere observed by NOZOMI. The dipole magnetic field lines of L = 4 and 5 are also shown. While the inner magnetic field line corresponds to the plasmapause, the outer magnetic field line corresponds to the outer boundary of the dusk bulge [*Yoshikawa et al.*, 2000a].

Recent advances in satellite-based imaging techniques have made it possible to routinely obtain full global images of the plasmasphere. The Extreme Ultraviolet Imager (EUV) on the Imager for Magnetopause-to-Aurora Global Exploration (IMAGE) satellite gave us complete sequential pictures [*Burch et al.*, 2001a, 2001b; *Sandel et al.*, 2000, 2001]. The EUV instrument detects the distribution of He^+ in the plasmasphere with a time resolution of 10 min and a spatial resolution of 0.1 R_E at the apogee (~8 R_E). The EUV instrument consists of three sensor heads and their fields of view are joined to create a single image.

The EUV images of the plasmasphere reveal a host of distinct features and behaviors [*Sandel et al.*, 2001, 2003]. Figure 1.7 shows an example of the EUV images. The sun is toward the lower right, and the Earth's shadow extends through the plasmasphere in the opposite direction, toward the upper left. The sharp drop of intensity corresponds to the plasmapause. This image also illustrates some aspects of the plasmasphere that have proven especially accessible by EUV imaging techniques, a shoulder (lower center), a drainage plume (right), and a pre-midnight channel (top).

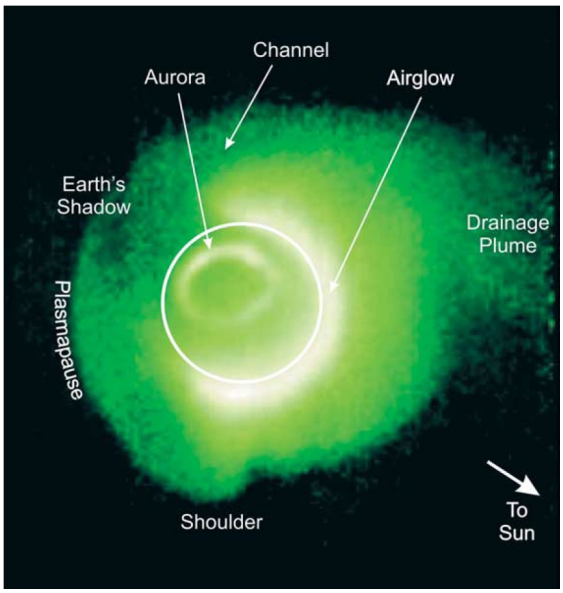

Figure 1.7: Two-dimensional imagery observed by Extreme Ultraviolet Imager onboard the IMAGE satellite on 24 May 2000, during a magnetic storm. A drainage plume extends sunward past the right edge of the image. The Earth's shadow is visible in the direction away from the Sun, because only He^+ illuminated by the Sun scatters the target wavelength. The white circle shows the approximate size and position of the Earth [*Sandel et al.*, 2003].

The recent imaging instruments in the EUV region mentioned above have similar types of optics. Figure 1.8 shows schematic cross-sectional drawings of (a) the XUV scanner onboard the Planet-B spacecraft and (b) one of the EUV sensor heads onboard the IMAGE satellite. Each instrument is both designed as a type of normal-incidence telescope. Their optics consists of a multilayer coated mirror to focus EUV photons, a metal thin filter to eliminate unwanted longer wavelength emissions, and microchannel plates to pick up photon events.

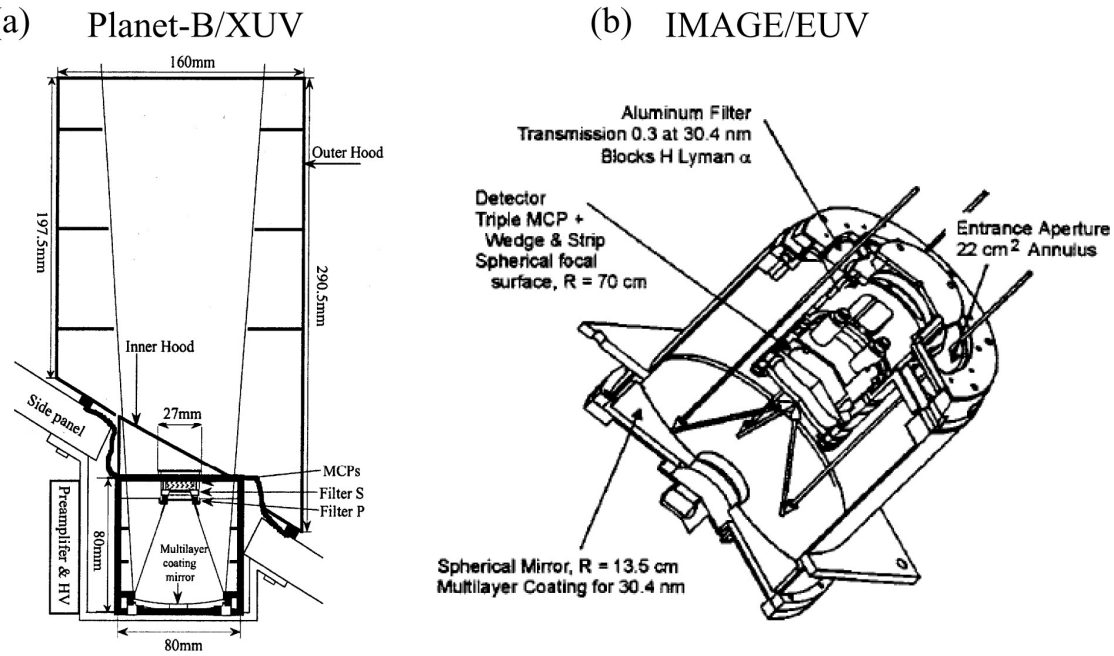

Figure 1.8: (a) A schematic cross-sectional drawing of the XUV scanner onboard the Planet-B (Nozomi) spacecraft [*Nakamura et al.*, 2000]. The optics consists of a multilayer-coated mirror, a thin metal filter, and microchannel plates. (b) **A c**utaway drawing of the EUV sensor onboard the IMAGE satellite [*Sandel et al.*, 2000].

In the near future, an instrument which has a similar type of optics to those onboard Planet-B and IMAGE will take global images of the plasmasphere from the lunar orbit. The Selenological and Engineering Explorer (SELENE) was launched by the H-IIA rocket in September of 2007 and then put into the orbit around the Moon. The Telescope of Extreme Ultraviolet (TEX) mounted in the Upper atmosphere and Plasma Imager (UPI) on SELENE detects the resonance scattering emissions of oxygen ions (O

II: 83.4 nm) and helium ions (He II: 30.4 nm) to take images of near-Earth plasmas. The UPI-TEX imager has a time resolution of 1 minutes and a spatial resolution of 0.1 R_E. The observation of the plasmasphere by UPI-TEX from the lunar orbiter will give us not only much more sequential images with higher time resolution but also a deeper understanding of the plasmasphere dynamics from a different perspective.

1.3 Construction of this Thesis

The main purpose of this thesis is to examine the plasmasphere dynamics by means of a global imaging technique in the extreme ultraviolet (EUV) spectral range. This thesis consists of 5 chapters. Chapter 2 presents the statistical research on the plasmapause response to the southward turning of the IMF observed by the Extreme Ultraviolet Imager (EUV) onboard the IMAGE satellite. In Chapter 3, the detailed description of the Telescope of Extreme Ultraviolet in the Upper atmosphere and Plasma Imager (UPI-TEX) onboard the SELENE satellite is presented. Chapter 4 includes the characteristics of the newly developed high-resolution imaging detector using five microchannel plates (MCPs) and a resistive anode encoder (RAE) for the future missions. Concluding remarks are given in Chapter 5.

2 The Plasmapause Response to the Southward Turning of the IMF Derived from Sequential EUV Images

2.1 Introduction

The plasmapause is the outer boundary of the Earth's plasmasphere which is a torus-shaped region filled with cold plasmas in the inner magnetosphere. Decades of observation show that the radial location of the plasmapause generally moves inward during geomagnetic disturbance periods. The inward motion is explained by a longstanding hypothesis that the dynamics of the plasmasphere is controlled by the superposition of the corotation and convection electric field [*Nishida*, 1966]. The enhanced convection electric field triggered by the southward turning of the IMF forms new $E \times B$ drift trajectories, and plasmas on the plasmapause move inward along them [*Chappell et al.*, 1970].

Some other mechanisms explaining the inward motion of the plasmapause during geomagnetic disturbance periods have been proposed. *Lemaire* [1974, 1985] proposed that the centrifugal force drives the plasma upwards and then produces a sharp density gradient along the magnetic field lines tangent to the zero parallel force (ZPF) surface. According to this mechanism, after an increase in the level of magnetic activity the ZPF surface shifts inward and the plasmasphere is peeled off in the post midnight sector where the convection velocity is maximum [*Lemaire and Gringauz*, 1998]. *Carpenter and Lemaire* [1997] discussed the loss of plasmas through the flow from the plasmasphere into the underlying ionosphere during periods of the enhanced convection. They indicated the possibility of the mechanism involving dumping of plasmas into the ionosphere based on the whistler data.

Although it is not completely understood how the convection electric field governing the dynamics mentioned above propagates to the inner magnetosphere, a number of observational studies have examined the ionospheric response to the IMF. For example, the ionospheric convection responds to the IMF quickly (~10 min) [*Ridley et al.*, 1998] and almost simultaneously at the whole ionosphere [*Kikuchi et al.*, 1996; *Ruohoniemi and Greenwald*, 1998; *Ridley et al., 1998*; *Lu et al.*, 2002]. Furthermore, using the ground magnetometers, *Hashimoto et al.* [2002] examined the response time of the convection in the inner magnetosphere to the enhancement of the ionospheric convection. Their study suggests that the convection electric field propagates from the

dayside magnetopause to the nightside inner magnetosphere through the ionosphere.

With regard to experimental work on the plasmasphere, the conventional extreme ultraviolet (EUV) photometric experiments from an inside-out view, which had been done intensively in the 1970s, suggested that the Earth's plasmasphere would be imaged by He II (30.4 nm) emission [e.g., *Johnson et al.*, 1971]. In the 1990s, the remote sensing method using the EUV emission became a powerful tool to provide global perspectives on the plasmasphere dynamics [*Williams et al.*, 1992]. The fundamental technology to detect the EUV emission began with the He II emission through a rocket experiment [*Yoshikawa et al.*, 1997]. The two-dimensional He II imaging of the terrestrial plasmasphere from its outside was first done by the Planet-B (Nozomi) spacecraft [*Nakamura et al.*, 2000]. *Yoshikawa et al.* [2000a, 2000b, 2001] first presented static EUV images of the plasmasphere and the inner magnetosphere.

Recent advances in satellite-based imaging techniques have made it possible to routinely obtain full global images of the plasmasphere. The EUV instrument on the Imager for Magnetopause-to-Aurora Global Exploration (IMAGE) satellite gave us complete sequential pictures (one image/10 min) [*Burch et al.*, 2001a, 2001b; *Sandel et al.*, 2000, 2001]. Using these sequential images, *Goldstein et al.* [2003b, 2003c, 2004a, 2005] and *Spasojević et al.* [2003] identified the correlation between the inward motion of the plasmapause and the southward turning of the IMF for specific events. They found that the timescale of the plasmapause response to the IMF is about 30 min in their case studies. Furthermore, *Pierrard and Cabrera* [2005, 2006] presented the simulations of the plasmapause formation and compared the predicted plasmapause positions with the EUV observations. They remarked the correlation between the inward motion of the plasmapause and the southward turning of the IMF in numerical simulations. However, they did not discuss the timescale of the plasmapause response to the IMF in their studies.

In this study, I statistically examine the plasmapause response to the southward turning of the IMF in order to understand the propagation mechanism of the convection electric field in the inner magnetosphere. I survey the EUV data set in the period of May 2000–December 2001 obtained by the IMAGE satellite (http://euv.lpl.arizona.edu/euv/), and find the events showing the clear inward motion of the nightside plasmapause. Finally, the timescale of the plasmapause response to the southward turning of the IMF is deduced.

2.2 Data Selection

The EUV instrument on the IMAGE satellite imaged the He^+ distribution in the plasmasphere by detecting resonantly scattered solar 30.4-nm radiation. The measured brightness is directly proportional to the He^+ column density along the line of sight because the 30.4-nm emission from the plasmasphere is optically thin [*Sandel et al.*, 2001]. The EUV imager consisted of three cameras, and their fields of view were overlapped to create a single image. It produced sequential images of the plasmasphere every 10 min for generally 7−9 hours out of each 14-hour orbit, with spatial resolution of ~0.1 R_E as seen from the apogee (~8 R_E).

The EUV instrument sometimes observed the inward motion of the nightside plasmapause driven by the southward IMF, called as erosion, in a time series of global snapshots [*Goldstein et al.*, 2003b, 2003c, 2004a, 2005; *Spasojević et al.*, 2003]. Figure 2.1 shows sequential images of the plasmasphere (one image/10 min) taken by the EUV instrument on 22 April 2001. In each image the direction of the Sun is to the upper left and the dotted circle represents the Earth. The left side data in each image are not available because throughout the event the camera whose field of view covered the duskside was usually turned off to prevent sunlight from entering the camera [*Goldstein et al.*, 2005]. In this period it is clear that the nightside plasmapause, especially at post midnight (the lower right), become sharper and move inward by ~1.5 R_E.

To investigate the inward motion of the plasmapause driven by the southward turning of the IMF, I searched the EUV data set in the period of May 2000-December 2001, and identified 16 events according to the following criteria:

–The northward IMF continued more than 10 min before the southward turning.

–The IMF turned southward more rapidly than 0.25 nT/min.

–The southward IMF continued more than 10 min after the turning.

–The EUV instrument clearly observed the sharp plasmapause on the nightside and the whole inward motion of the nightside plasmapause in the field of view.

Figure 2.2 shows an example of the variation of the IMF B_Z component (B_{IMF_Z}) satisfying the above criteria, measured by the MAG instrument onboard the ACE satellite [*Smith et al.*, 1998] on 22 April 2001. The IMF turned southward at 01:27 and 02:15 UT distinctly. I used 1-min interval data set of the IMF. The arrival time of every IMF at the average magnetopause (10 R_E) from the ACE position was estimated

as follows.

(1) It was assumed that the every IMF measured by the MAG instrument continued to propagate and arrived at the magnetopause and that the magnitude and polarity of the IMF did not change.

(2) I used the solar wind velocity data simultaneously measured by the SWEPAM instrument on the ACE satellite [*McComas et al.*, 1998] and assumed the velocity did not change. The arrival time of every IMF at the magnetopause was calculated based on the position of the ACE satellite.

(3) Every IMF was labeled the arrival time at the magnetopause. This method provides more correct information than by simply assuming a constant velocity of the solar wind.

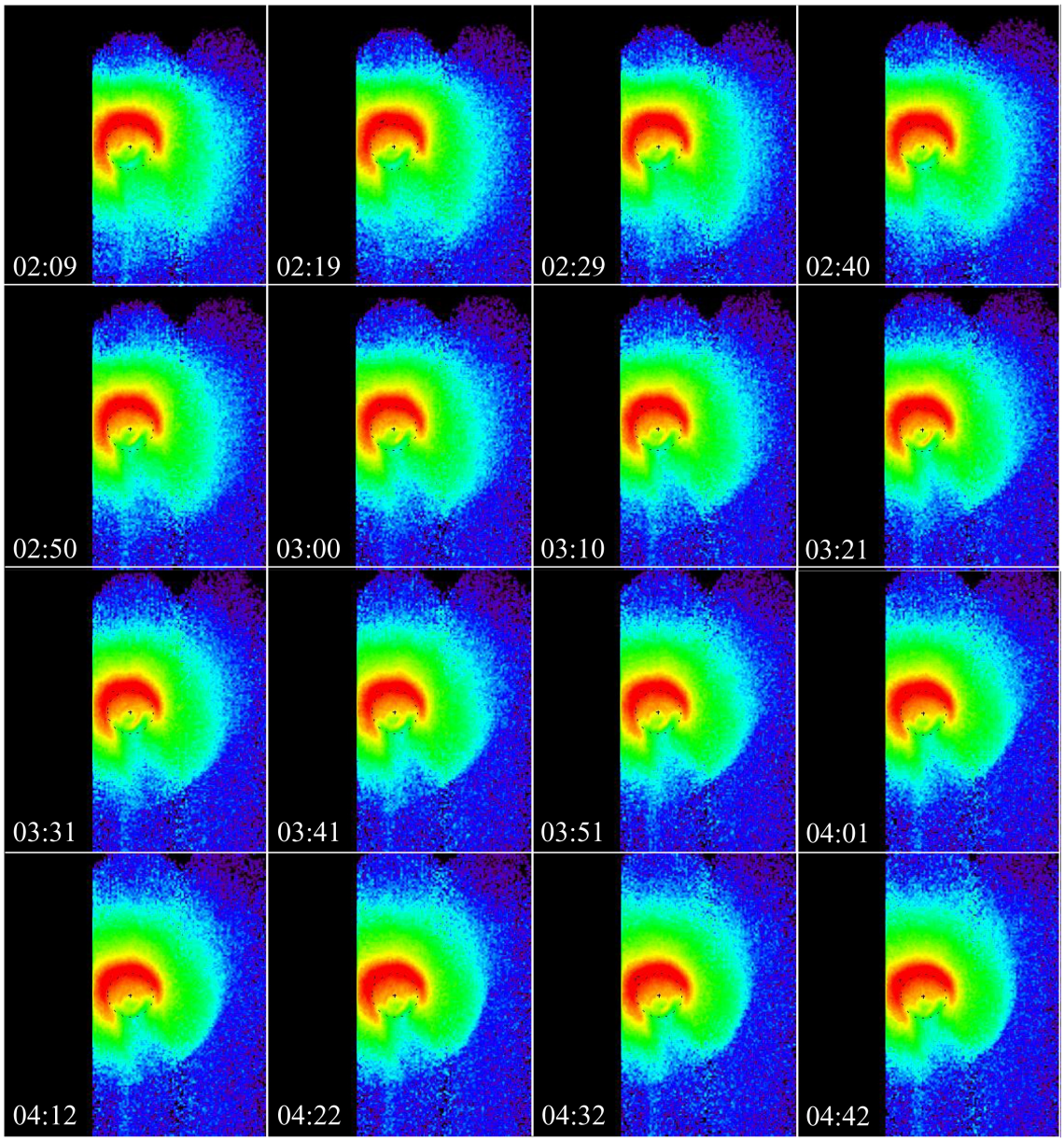

Figure 2.1: Sequential images of the plasmasphere taken by the EUV instrument onboard the IMAGE satellite on 22 April 2001. In each image the direction of the Sun is to the upper left and the dotted circle represents the Earth. Each image is 10 min apart. The left side data in each image are not available throughout the event. In this period the nightside plasmapause is found to be sharp and move inward by about 1.5 R_E.

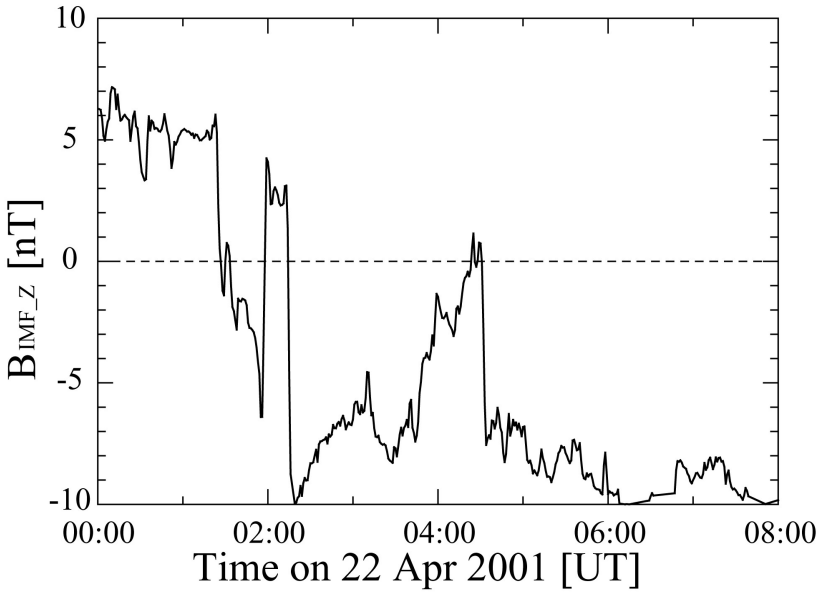

Figure 2.2: The 1-min interval data set of the IMF B_Z component (in GSM coordinates) on 22 April 2001 measured by the MAG instrument onboard the ACE satellite. The arrival time of every IMF has been compensated at the average magnetopause (10 R_E) from the ACE position (~213 R_E), taking into account the variation of the solar wind velocity.

2.3 Analysis

Figure 2.3a shows two snapshots of the He^+ plasmasphere taken at 02:29 and 04:32 UT on 22 April 2001 by the EUV imager. They are also included in Figure 2.1. The black circle indicates the Earth and the white arrow points sunward in each image. The shadow of the Earth is seen in the antisunward direction, and the bright arc at the Earth's dayside limb is airglow from He and O^+ [*Burch et al.*, 2001a, 2001b]. The left side data are not available as explained in the previous section. The white squares indicate the manually identified plasmapause along the sharp brightness gradient. In Figure 2.3a, the sharp He^+ edge is identified in the EUV image, and it corresponds to the plasmapause [*Roelof and Skinner*, 2000; *Goldstein et al.*, 2003a].

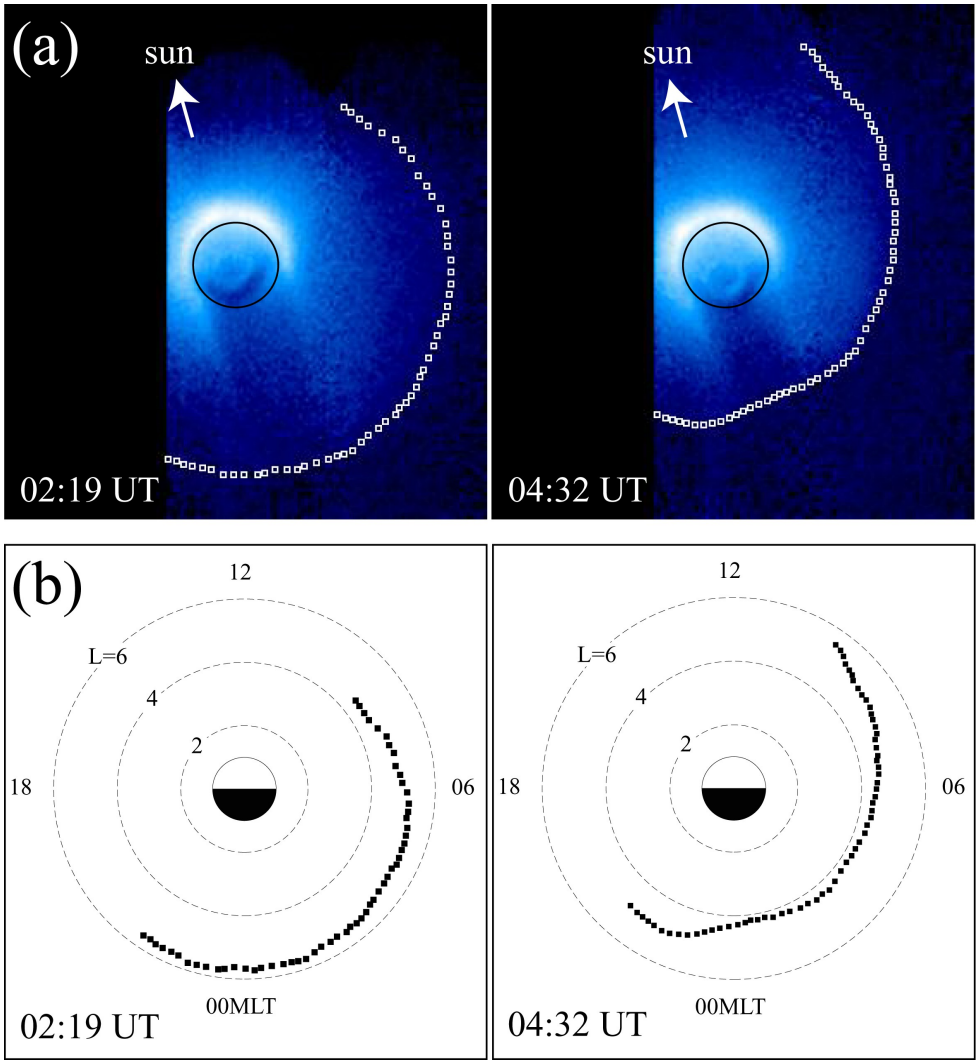

Figure 2.3: (a) Images of the He^+ plasmasphere taken by the EUV instrument on 22 April 2001. The black circle indicates the Earth and white squares indicate the manually identified plasmapause in the EUV images. The left side data are not available. (b) The plasmapause of each image mapped to the magnetic equatorial plane. The black squares indicate the manually identified plasmapause in the magnetic equatorial plane, and the dashed circles are drawn at L = 2, 4, 6. The nightside plasmapause at 04:32 UT is about $1.5R_E$ closer to the Earth than that at 02:29 UT.

On the assumption that the plasmapause is field aligned in the dipole magnetic field, the field line with the minimum L (radial distance in the equatorial plane) along the line of sight to each identified point is found, as shown in Figure 2.4. Then the plasmapause can be mapped to the magnetic equatorial plane along the field line, like

Goldstein et al. [2003a]. There is some subjectivity involved in manually extracting the plasmapause. This manual extraction of the plasmapause was repeated and the dispersion of the identified plasmapause locations was calculated. As a result, the uncertainty due to the subjectivity was estimated to be about 0.2 R_E, which is consistent with that reported in *Goldstein et al.* [2003a, 2005]. Figure 2.3b shows the plasmapause locations at 02:29 and 04:32 UT on 22 April 2001 mapped to the magnetic equatorial plane using this method. It is clear that the nightside plasmapause at 04:32 UT is about 1.5 R_E closer to the Earth than that at 02:29 UT in Figure 2.3b.

The plasmapause radial velocity (V_{pp}) was calculated after mapping the plasmapause in the EUV images to the equatorial plane. Using centered time differencing of the sequential plasmapause positions, V_{pp} was calculated at the particular MLT where the plasmapause was clearly identified and the inward motion was most pronounced. For example, Figure 2.5 shows the variation of V_{pp} at 2.1 MLT on 22 April 2001. V_{pp} has the subjective error due to the subjectivity in manually extraction of the plasmapause (0.2 R_E) as mentioned in the previous section. Using this value, the average uncertainty in V_{pp} was estimated to be about ±0.4 R_E/hour, which is consistent with that discussed by *Goldstein et al.* [2003a, 2003b]. As seen in Figure 2.2 and Figure 2.5, B_{IMF_Z} and V_{pp} have very similar variations with a time lag.

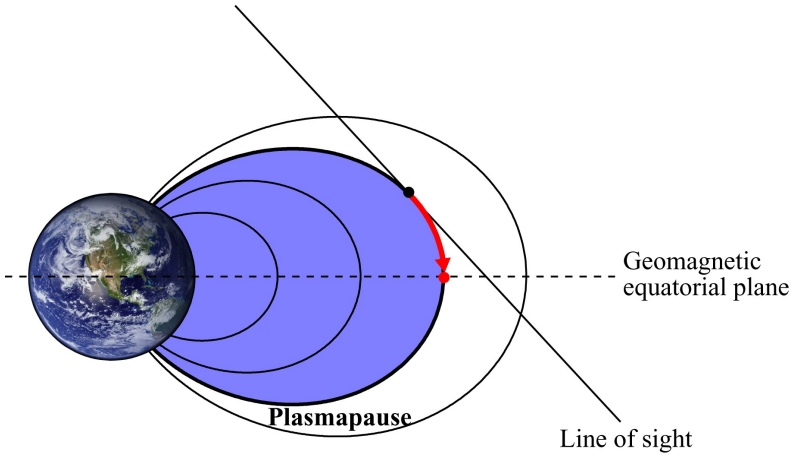

Figure 2.4: A schematic diagram of the plasmasphere and the line of sight of EUV in the meridional plane. The plasmapause in the EUV images was mapped to the geomagnetic equatorial plane as follows. The points corresponding to the plasmapause (black dot) are manually selected along the sharp brightness gradient on each image. Next, the minimum L along the line of sight is found for each selected point, and the field line is traced to the magnetic equator (red dot).

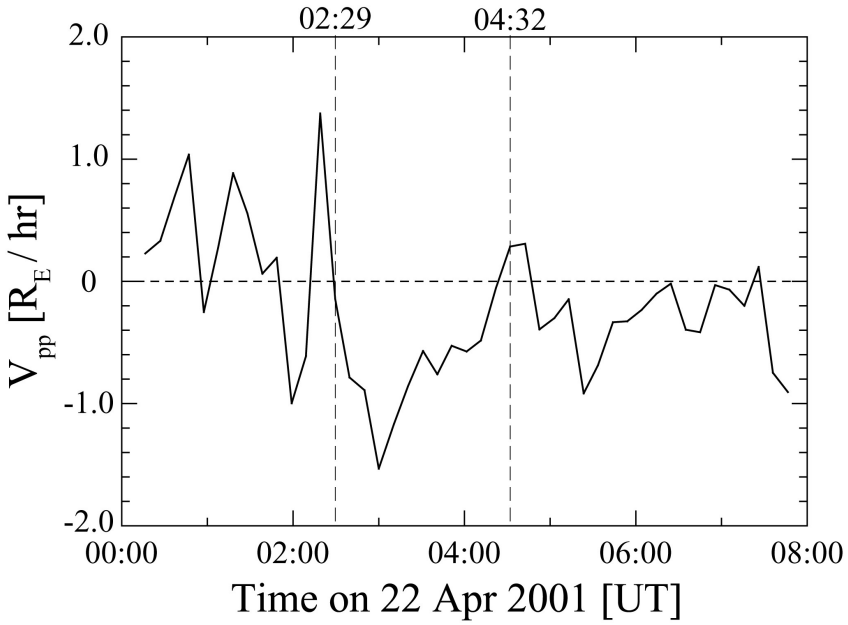

Figure 2.5: Radial plasmapause velocity (V_{pp}) on 22 April 2001 at 2.1 MLT where the inward motion of the nightside plasmapause was most pronounced. $V_{pp} < 0$ indicates that the plasmapause moves inward. The prominent inward motion of the plasmapause occurs in the period between 02:29 and 04:32 UT, and the locations of the plasmapause at both times are presented in Figure 2.3. The error of V_{pp} due to the manually extraction of the plasmapause is about ±0.4 R_E/hour.

The solar wind and IMF impose an electric field potential across the magnetosphere, driving the convection. Therefore to examine the correlation between the plasmapause motion and the IMF turning, it is meaningful to express both in electric field parameters. On the assumption that the plasmas on the plasmapause move by $E \times B$ drift (see Figure 1.5), the plasmapause motion is represent as the electric field parameter (E_{pp}) defined as

$$E_{pp} \equiv V_{pp} \times B_{dipole}, \tag{2.1}$$

where B_{dipole} is the equatorial dipole geomagnetic field. I calculate B_{dipole} using a simple dipole formula, $B_{dipole} = B_E/L^3$ ($B_E = 3.11 \times 10^5$ T). E_{pp} approximately corresponds to the convection electric field in the midnight region. The variation of E_{pp} is dominated by that of V_{pp} because B_{dipole} is smooth. Similarly, the variation of the IMF is represented as the electric field of the solar wind (E_{sw}) defined as

$$E_{sw} \equiv V_{sw} \times B_{IMF\_Z}, \tag{2.2}$$

where V_{sw} is the solar wind velocity. I used V_{sw} data measured by the SWEPAM instrument onboard the ACE satellite.

Then I calculated the linear correlation coefficient between E_{pp} and E_{sw} with various time delays, to investigate the response time of the plasmapause to the IMF. Figure 2.6 shows the correlation coefficient on 22 April 2001. The maximum value of the correlation is 0.73 when a 16-min delay is assumed. Because of the interval of the EUV data set (10 min) and the subjective error in V_{pp}, the response time calculated in my method has some uncertainty. For reference, therefore, the range of 90% of the maximum correlation value is displayed in Figure 2.6. Both E_{pp} and 16-min delayed E_{sw} are shown in Figure 2.7, where E_{pp} multiplied by 5 is displayed to show both quantities in the same magnitude. The number of 5 suggests that the solar wind electric field penetrates in the inner magnetosphere by 20%. This is consistent with the result of 10–25% reported in previous studies [*Goldstein et al.*, 2003b, 2003c, 2004b, 2005]. As seen in Figure 2.7, E_{pp} and E_{sw} are clearly correlated.

For the other events, the correlation coefficients were calculated in the same way. Table 2.1 and Figure 2.8 show the results. The best-correlated time delay between E_{pp} and E_{sw} is regarded as the timescale of the plasmapause response to the IMF variation. There are four events in which the maximum values of the correlation coefficient are below 0.5 in Table 2.1. Among four events, there is common aspect that the IMF has a shortly periodical structure and therefore there are several local maximum values in the correlation coefficient. That decreases the overall maximum value in the correlation coefficient. Nevertheless, these events also imply that the plasmapause responded to the southward turning of the IMF. These four events are included in my results. Finally, my results indicate that the plasmapause response to the southward turning of the IMF takes 10–30 min, and average 18 min.

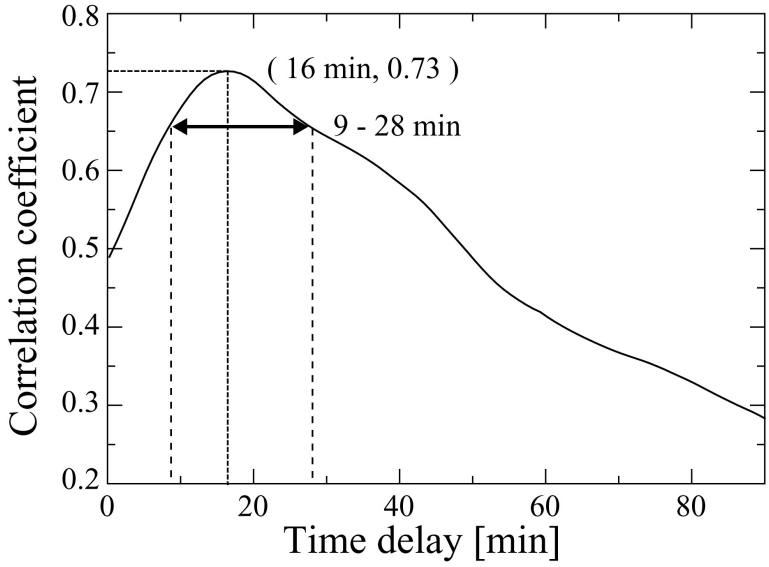

Figure 2.6: The correlation coefficient between the electric field parameters at the plasmapause (E_{pp}) and in the solar wind (E_{sw}) on 22 April 2001. The maximum value of the correlation is 0.73 at a 16-minute delay. The range of 90% of the maximum correlation value is also displayed.

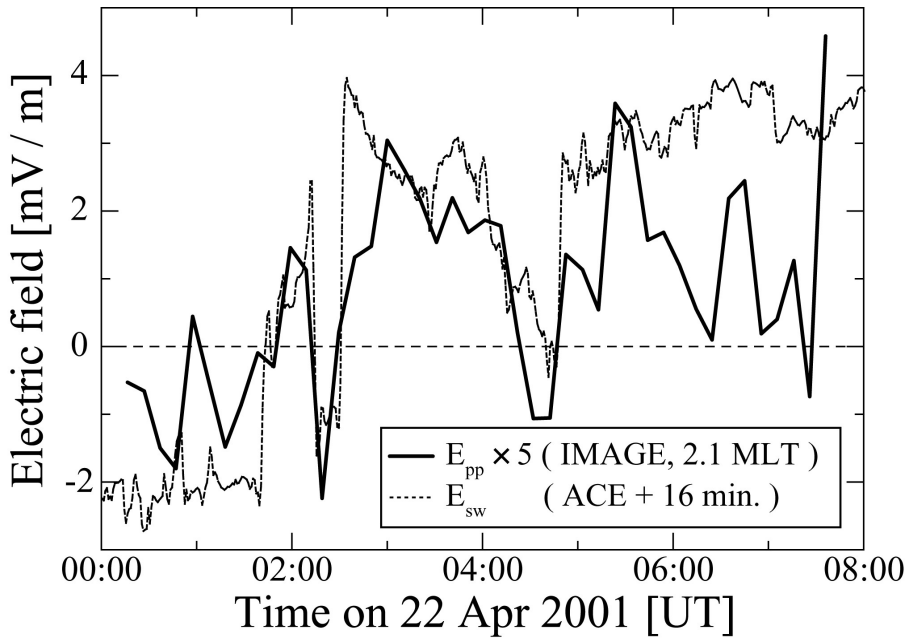

Figure 2.7: Electric field parameters E_{pp} (plasmapause) and E_{sw} (solar wind). The variations of E_{pp} and E_{sw} are qualitatively the same as V_{pp} and B_{IMF_Z}, respectively. E_{sw} is displayed with 16-minute delay, which is the best correlated time delay between Epp and E_{sw}. E_{pp} has been multiplied by 5 in order to show both quantities in the same magnitude.

Table 2.1: The event list showing the date, MLT where the radial plasmapause velocity was calculated, the maximum value of the correlation coefficient between Epp and Esw, the best correlated time delay, time delay variation among 90% of the maximum correlation value, the solar wind (SW) propagation time from the ACE satellite to the magnetopause in this study, and previously published studies

Date	This study					Previous case study	
	MLT	Correlation	Delay (min)	90% range (min)	SW propagation (min)	Delay (min)	SW propagation (min)
29 May 2000	4.0	0.79	**21**	16 - 27	61		
2 Jun 2000	0.0	0.67	**23**	18 - 28	54		
3 Jun 2000	0.2	0.46	**0**	0 - 20	57		
8 Jun 2000	3.0	0.47	**22**	17 - 27	44		
10 Jul 2000	2.0	0.68	**28**	13 - 41	60	30[a]	63[b]
28 Jul 2000	0.4	0.51	**23**	19 -28	56		
5 Aug 2000	0.0	0.49	**19**	13 - 26	51		
17 Aug 2000	2.0	0.54	**19**	7 - 33	62		
28 Aug 2000	1.5	0.58	**13**	7 - 21	43		
6 Feb 2001	1.6	0.66	**10**	3 - 34	70		
22 Apr 2001	2.1	0.73	**16**	9 - 28	60	27[c]	63
28 May 2001	2.8	0.51	**18**	0 - 38	46		
1 Jun 2001	3.0	0.59	**0**	0 - 26	71		
2 Jun 2001	1.0	0.59	**24**	18 - 32	58	32[d]	55
21 Jun 2001	3.0	0.58	**15**	6 - 27	43		
26 Jun 2001	3.0	0.45	**29**	24 - 50	52	32[e]	54.8

[a]: [*Goldstein et al.*, 2003b]

[b]: *Goldestein et al.* [2003b] used the IMF data set measured by the Geotail satellite. They assumed the constant solar wind velocity of ~400 km/s and calculated the solar wind propagation time by 3.7 min based on the Geotail position (~24 R_E). I extrapolated the propagation time from the ACE position (~238 R_E).

[c]: [Goldstein et al., 2005]

[d]: [Goldstein et al., 2003c, 2004a]

[e]: [Spasojević et al., 2003]

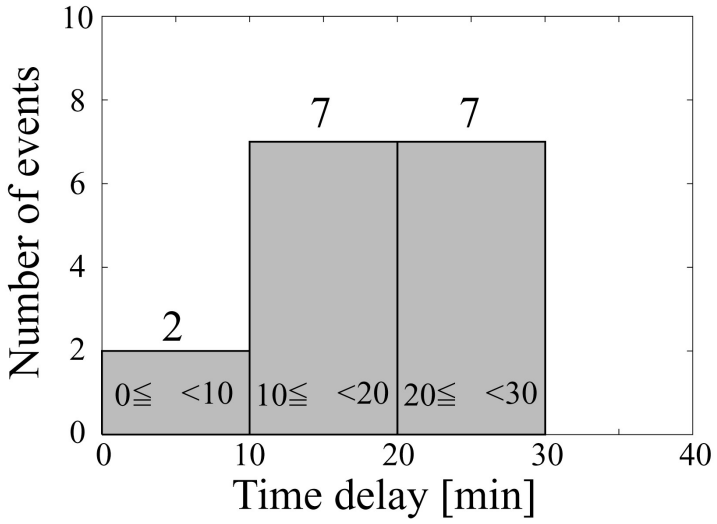

Figure 2.8: The histogram of the time delay between E_{pp} and E_{sw} listed in Table 2.1. It corresponds to the response time of the plasmapause to the IMF variation.

2.4 Discussion

The timescale of the plasmapause response to the southward turning of the IMF derived from the sequential EUV images was studied for specific events. Table 2.1 shows the results of the previously published case studies. For example, *Goldstein et al.* [2003b] found that the response time on 10 July 2000 is 30 min at 2.4 MLT, while it is 28 min at 2.1 MLT in this study. Also, *Spasojević et al.* [2003] reported that on 26 June 2001, the response time is 32 min, and by my method it is 29 min. The results of my research for these two events are consistent with those of their case studies. However, as shown in Table 2.1, the response times on 2 June 2001 and 22 April 2001 in my results are different from those reported by *Goldstein et al.* [2003c, 2004a] and *Goldstein et al.* [2005] by ~10 min. In spite of using almost the same techniques to determine the response time of the plasmasphere to the IMF as theirs, my estimates show shorter response times than those in their studies. These discrepancies would mainly result from the difference in the method to compensate the propagation time of the IMF from the satellite to the magnetopause. *Goldstein et al.* [2003c, 2004a, 2005] assumed the constant solar wind velocity. I also calculated the response time using their method and found the same result. But in order to calculate the correlation more precisely, I took into account the variation of the velocity.

The plasmapause response to the southward turning of the IMF provides

important information about the complex coupling of the inner/outer magnetosphere, ionosphere, and solar wind. In this chapter, I have shown that the convection electric field is rapidly distributed in the inner magnetosphere within 10-30 minutes, based on the sequential EUV images of the plasmasphere. The rapid response of the convection electric field to a sudden change in the IMF is discussed.

In recent years, many authors have argued the quick response of the plasma convection in the ionosphere [e.g., *Hairston and Heelis*, 1995; *Ruohoniemi and Greenwald*, 1998; *Ridley et al.*, 1998; *Lu et al.*, 2002]. *Ridley et al.* [1998] investigated the electric potential in the ionosphere using the ground magnetometers, and found that the ionospheric convection starts to change with a time lag of 8.4–13.6 min (Δt_1) from the arrival of the IMF at the magnetopause. Furthermore, the progress of global observations by magnetometers and radars with high temporal resolution enable us to investigate the response of the ionospheric convection over a wide range of local times and latitudes simultaneously. In the recent studies of the ionospheric convection, it has been shown that the convection starts almost simultaneously ($\Delta t_2 < 2$ min) at all magnetic local time [e.g., *Ruohoniemi and Greenwald*, 1998; *Lu et al.*, 2002] and at whole latitudes [*Kikuchi et al.*, 1996].

Following to these results, *Hashimoto et al.* [2002] studied a quick response of the magnetospheric convection to sudden IMF changes and the development of partial ring current by using the ground magnetometer data obtained from the polar cap to low-middle latitude stations. They demonstrated that the response time of the convection in the inner magnetosphere to the enhancement of the ionospheric convection takes 5–11 min (Δt_3). Based on this result, they suggested that the convection electric field propagates from the dayside magnetopause to the nightside inner magnetosphere through the ionosphere.

The timescale (Δt_{total}) that the convection electric field takes to propagate to the inner magnetosphere through the mechanism mentioned above can be estimated to be 13-27 min, based on the past observational studies as follows: $\Delta t_{total} = \Delta t_1 + \Delta t_2 + \Delta t_3$. This timescale is consistent with the time lag of 10-30 min between the southward turning of the IMF and the plasmapause motion. Therefore, this study suggests that the convection electric field penetrates from the magnetopause to the inner magnetosphere through the ionosphere. But this is not an exclusive mechanism. Further study is necessary.

2.5 Summary

Using the sequential images of the plasmasphere observed by the EUV instrument on the IMAGE satellite, I examined the plasmapause dynamics. I have shown that the plasmapause response to the southward turning of the IMF takes 10–30 min, and average 18 min. It is consistent with the timescale derived from the ionospheric observations. Therefore it indicates that the electric field penetrates from the magnetopause to the inner magnetosphere through the ionosphere. However, due to the limited EUV data, only 16 events were found in my search. Future observation of the plasmasphere by the SELENE satellite from the lunar orbit will give us not only much more sequential images with higher time resolution but also a deeper understanding of the plasmasphere dynamics from a different perspective.

3 Calibration of Telescope of Extreme Ultraviolet (TEX) onboard SELENE

3.1 Introduction

Our knowledge of the Earth's plasmasphere has increased steadily owing to a number of *in-situ* plasma measurements during the past several decades. The plasmasphere is filled with cold ions such as H^+, He^+, and a small amount of O^+ and is filled up to high density (about 100 ions/cm^3). The outer boundary, the plasmapause, is interpreted as a separatrix between closed and open convection trajectories [*Nishida*, 1966]. Under a steady convection electric field condition, the plasmapause is considered to form a "teardrop" shape on the equatorial plane. The traditional models indicate that the plasmapause moves closer to the Earth when the large-scale convection electric field is enhanced. The plasma which was previously on a closed drift path then changes to an open drift path. As a result, the open drift path carries the plasma sunward, creating a plasmaspheric tail [*Chen and Wolf*, 1972] or a detached plasma region [*Chappell*, 1974]. One question concerning the existence or nonexistence of such a structure has remained unresolved because the conventional *in-situ* observations for cold ions have an inherent shortcoming. The *in-situ* observations provide only local information, which does not include the necessary global aspect of the plasmasphere. It is therefore difficult to draw a definite conclusion on the above question. Global-scale observation is, therefore, a natural extension to many years of single-point *in-situ* observations. The primary motivation of this field of science is to visualize the global shape of the plasmasphere.

Standard theories on the polar wind indicate that only light ions such as H^+ and He^+ can overcome the terrestrial gravitational potential to escape from the polar ionosphere due to a pressure gradient along open field line and that the O^+ outflow is limited due to both its large mass and its loss by charge exchange with neutral H in the atmosphere [e.g., *Axford*, 1968; *Banks and Holzer*, 1968]. Observations by polar orbiting satellites such as Dynamic Explorer 1 (DE-1) and AKEBONO (EXOS-D), however, found that the upward flux of O^+ is comparable to that of H^+, especially under an active geomagnetic condition and during a period of a high solar activity [e.g., *Chandler et al.*, 1991; *Abe et al.*, 1993, 1996]. Furthermore, GEOTAIL observed the cold dense O^+ flow of the ionospheric origin in the distant tail lobe [*Seki et al.*, 1996, 1999, and references therein]. The difference between the rate of O^+ outflow from the

polar ionosphere and that of O^+ escape from the magnetosphere to interplanetary space indicates that there should be as-yet unknown transport processes for O^+ in the magnetosphere [*Seki et al.*, 2001]. The two-dimensional (2-D) O II imagery, which provides a global O^+ distribution, is expected to identify the transport routes and mechanisms of the cold O^+ ions and to reveal a quantitative balance between supply and loss, including thermal plasma.

The remote-sensing methods using the extreme ultraviolet (EUV) emissions of He^+ (He II 30.4 nm) and O^+ (O II 83.4 nm) have been expected to be a powerful tool to provide global perspectives on the escaping processes [*Chiu et al.*, 1986; *Meier*, 1991; *Williams et al.*, 1992] because conventional *in-situ* plasma particle measurement methods cannot detect plasma particles far from the satellite or thermal plasmas. The fundamental technology used to detect He II emission began with the rocket experiments in the 1970s and 1980s [*Ogawa and Tohmatsu*, 1971; *Meier and Weller*, 1972; *Paresce et al.*, 1974; *Chakrabarti et al.*, 1982]. The measurements obtained using this technology clarified that the optical thickness of He^+ ions is very thin and that the intensity is very low (10 Rayleigh at most). They also clearly showed the feasibility of imaging the distribution of plasma around the Earth. In the 1990s, technological developments in EUV optics were reported in several articles [*Cotton et al.*, 1993; *Chakrabarti*, 1993], and a breakthrough in the multilayer coating technique was first demonstrated by the sounding rocket experiment [*Yoshikawa et al.*, 1997]. The 2-D He II imaging of the terrestrial plasmasphere from the outside was subsequently accomplished by both the Planet- B (Nozomi) spacecraft [*Nakamura et al.*, 2000; *Yoshikawa et al.*, 2000a, 2001] and the Imager for Magnetopause-to-Aurora Global Exploration (IMAGE) mission [*Burch et al.*, 2001a, b; *Sandel et al.*, 2001]. Cold He^+ ions in the near-Earth plasma sheet were also optically observed by Planet-B [*Yoshikawa et al.*, 2000b].

Optical observations on oxygen ions around the Earth have not yet been performed because of the difficulty in rejecting the bright H Ly-α line from the geocorona. The primitive equipment, denoted the eXtreme UltraViolet (XUV) sensor, was developed, that has thick indium film for the band-pass filter. The efficiency ratio of the O II emission to the H Ly-α line of this equipment is high enough to detect O II emission [*Yamazaki et al.*, 2002]. On December 4, 2000, this equipment flew onboard the sounding rocket SS-520-2 to investigate the mechanism of ion acceleration and/or

heating at the cusp/cleft region. The XUV sensor successfully detected O II emission from the uppermost part of the polar ionosphere. The altitudinal variation from 150 through 1100 km indicated the existence of O^+ ions beyond the polar ionosphere and suggested that the O^+ ions energized in the cusp/cleft region may drift to the uppermost part of the polar ionosphere.

An upgrade version of this instrument onboard the SELenological and ENgineering Explorer (SELENE) will obtain O II images of the polar wind and He II images of the plasmasphere from the lunar orbit. The SELENE was launched by the H-IIA rocket in 2007 to be put into the orbit around the Moon. The aims of the SELENE project are to carry out scientific observations of the Moon, at the Moon, and from the Moon. The Upper atmosphere and Plasma Imager (UPI) on SELENE takes 2-D visible and extreme ultraviolet images of atomic and plasma distribution in the upper atmosphere, ionosphere and around the Earth. The component has two telescopes; one is Telescope for VISible light (UPI-TVIS), and the other is Telescope for EXtreme ultraviolet light (UPI-TEX). The UPI-TVIS imager detects four emission lines (427.8, 557.7, 589.3, 630.0 nm) to simultaneously take auroral images around both of the Earth's polar regions. The UPI-TEX imager detects the resonance scattering emissions of oxygen ions (O II: 83.4 nm) and helium ions (He II: 30.4 nm) to take images of near-Earth plasmas. In this chapter the design of the UPI-TEX imager and its calibrated performance are presented.

3.2 Science Target

The UPI-TEX instrument provides global images of plasmas in the vicinity of the Earth by detecting He II (30.4 nm) emission scattered by He^+ ions and O II (83.4 nm) emission by O^+ ions. The observational targets are the plasmasphere and the polar wind. In the following subsections, the scientific motivations and open questions which have not been resolved by past satellite observations are presented.

3.2.1 Global Image of the Plasmasphere

The intensity of He II (30.4 nm) emission from the main body of the plasmasphere is reported as about 5 Rayleigh by *Nakamura et al.* [2000]. This result is consistent with early measurements of 1-10 Rayleigh done by sounding rockets from the inside-out view [e.g., *Ogawa and Tohmatsu*, 1971] and with simulated EUV images

of the plasmasphere [e.g., *Roelof et al.*, 1992]. The intensity from the outer boundary of the plasmasphere has not been clarified yet by the IMAGE mission, but reported to be in the range of 0.1-5 Rayleigh by the Planet-B satellite [*Yoshikawa et al.*, 2000a]. The intensity of 0.1-0.5 Rayleigh is considered to be a lower threshold level of the detection to grasp the global shape of the plasmasphere.

3.2.2 Plasmasphere Response to the Interplanetary Magnetic Field (IMF)

I used the sequential EUV images of the plasmasphere obtained by NASA's IMAGE satellite and investigated the plasmaspheric response time to the solar wind electric field that was measured by the solar monitor (the ACE satellite). It has been shown in Chapter 2 that the plasmapause response to the southward turning of the IMF takes 10–30 min, with an average of 18 min [also reported in *Murakami et al.,* 2007]. The result is consistent with the time scale derived from the ionospheric observations on ground stations [*Ridley et al.*, 1998; *Ruohoniemi and Greenwald*, 1998; *Lu et al.*, 2002; *Kikuchi et al.*, 1996; *Hashimoto et al.*, 2002]. Based on this accordance of data, I concluded that the electric field penetrates from the magnetopause to the inner magnetosphere through the ionosphere. However, the result should be re-investigated using a more completed data set of EUV images because only 16 events were found due to limited EUV data. The IMAGE satellite orbits near the Earth. As such, it cannot always monitor the whole plasmasphere, and there is always an interval of at least several hours between images, which makes it difficult to estimate the time lag between the IMF arrival at the magnetosphere and plasmasphere evolution. TEX observation improves this difficulty because SELENE provides the best platform to command a panoramic view of the whole plasmasphere. As cited above, the intensity of 0.1-0.5 Rayleigh is a lower threshold level to grasp the plasmaspheric response.

3.2.3 Plasmasphere Refilling

The refilling of the plasmasphere has attracted considerably theoretical interest for several decades [see "Plasmasphere Refilling" special section in *Journal of Geophysical Research*, 97(A2), 1047–1179, 1992]. Scientifically important studies on plasmasphere refilling were carried out in the 1960s and early 1970s. These were observational [*Park*, 1970; *Chappell et al.*, 1971] and theoretical and/or modeling studies [*Banks et al.*, 1971; *Schulz and Koons*, 1972; *Chen and Wolf*, 1972; *Grebowsky*,

1971] that addressed various refilling problems. One of the unsolved and highlighted issues is how plasma distribution approaches a diffusive equilibrium state under the condition of refilling, where plasma is supplied from the conjugate ionospheres through field-aligned supersonic flows. Most models dealing with refilling of the plasmasphere rely on initial conditions, such as plasma density, flow velocity, and temperature, in an empty flux tube. However, there is no theoretical basis to decide on the initial distributions, nor is there firm guidance from the observations. Because of the scarcity of information, the initial conditions are arbitrarily chosen in the models. The choice is generally only based on the fact that the equatorial plasma density in a depleted flux tube is as low as 1 cm^{-3}.

We do not know how this low equatorial density connects with the high ionospheric density. In this regard, systematic observation along a depleted flux tube should reveal the subsequent refilling process. It is impossible to carry out such observations, however, using a single satellite, because it is impossible to know latitudinal and longitudinal distributions of plasma simultaneously.

The EUV imaging is a promising methodology to overcome this difficulty. Based on the theoretical considerations, a time resolution of 30 min is necessary to examine the refilling issue [*Wilson et al.*, 1992]. The measured He II (30.4 nm) intensity of the refilling trough region is 0.02-0.1 Rayleigh as cited above. TEX should achieve this capability of time and spatial resolutions.

3.2.4 Continuous Leakage of Plasmaspheric Materials

Recent studies have revealed another feature of the plasmasphere. According to *in-situ* plasma measurements carried out on multiple geosynchronous satellites, the standard teardrop model of the plasmasphere, where the bulge size and location are determined by the convection electric field strength, is not a completely comprehensive description even under low geomagnetic activity [*Moldwin et al.*, 1994]. Furthermore, *Matsui et al.* [1999] have reported that GEOTAIL on a higher L value path (L~10) often found plasmaspheric materials independent of Kp. These researchers also concluded that cold plasma continuously moves toward the magnetopause. These results force us to verify the classical understanding and morphology of the plasmasphere/plasmapause that were constructed in the 1960s.

According to Matsui's statistical analysis, the structure of cold ions along the

GEOTAIL path (L>10) is quasi-stable, with a density of 2–10 cm^{-3}. If it is assumed that 10% of such a population consists of He^+ ions, that they spread along the dusk-to-dawn direction of 10 R_E, and that the g-factor of He II (30.4 nm) emission is 2×10^{-5} (ion^{-1} s^{-1}), then the intensity of He II (30.4 nm) from this source is estimated at 0.026-0.13 Rayleigh. Thus, it is necessary to construct optics with a lower threshold level of about 0.02 Rayleigh to identify this unique phenomenon.

3.2.5 Inconsistency of Old and New Topics on the Plasmasphere

The subject of the continuous leakage of cold plasma introduced in Section 3.2.4 may be related to the issue of plasmasphere refilling. On one hand, in recent studies, such as that of Matsui, it has been possible to determine the rate of ion leakage from the plasmasphere provided that the amount of plasma supplied directly from the ionosphere is not dominant. On the other hand, such as in studies of the plasmasphere refilling, it is difficult to determine the evolution of the content in the same flux tube from the *in-situ* observation, because a flux tube drifts regardless of a satellite orbital motion. The early measurements on the refilling rate of the ionospheric plasma may include the contribution of plasma leakage from the inner plasmasphere. Consequently, the refilling rate may be overestimated. The EUV observation provides promising clues for the verification of the above two processes—i.e., the plasmasphere refilling and a continuous leakage of plasmaspheric ions.

3.2.6 Net Escape Rate of Earth's Oxygen to Space

The observed polar outflow rate for O^+ ions corresponds to the loss of about 18% of the present-day atmospheric oxygen over 3 billion years. However, part of this apparent loss can actually be returned to the atmosphere. Examining loss rates of four already identified escape routes with high-altitude spacecraft observations, *Seki et al.* [2002] showed that the total oxygen loss rate inferred from current knowledge is about one order of magnitude smaller than the polar O^+ outflow rate. They then suggested that there might be a substantial return flux from the magnetosphere to the low-latitude ionosphere and also implied that this may indicate the existence of an as-yet unknown loss process for terrestrial oxygen. Otherwise, the net escape loss over 3 billion years may drop to about 2% of the current atmospheric oxygen content. This issue is very important not only for magnetosphere physics but also for the field of planetology.

Photometric observation is a very useful approach to resolve this issue as it is difficult to observe the escape of cold O^+ ions by *in-situ* measurements at energies below 50 eV without spacecraft potential control [*Seki et al.*, 2002].

3.2.7 Short- and Long-terms Variation of O^+ Outflow

Previous studies reported that the occurrence of the O^+ outflow event depends on the direction of the IMF, the geomagnetic activity, the seasonal condition, and the solar activity [e.g., *Chandler et al.*, 1991; *Abe et al.*, 1993, 1996]. *Chiu et al.* [1990] predicted the intensity of O^+ outflow to range from 0.3 to 1 Rayleigh. Recently the Low-Energy Neutral Atom imager (LENA) on IMAGE observed the oxygen ion burst outflow in response to an enhancement of the dynamic pressure of the solar wind at the moment of the passage of a shock produced by a coronal mass ejection [*Moore et al.*, 2001; *Fuselier et al.*, 2001]. These observations indicated that the O^+ outflow flux has both a long- and short-term variation; therefore, a constant monitoring and simultaneous observation of solar wind plasma are necessary to identify O^+ outflow mechanisms. The LENA imager can detect the energetic neutral atoms within the energy range of 10-750 eV [*Moore et al.*, 2000]. The TEX instrument, however, can detect the O II emission scattering by the thermal O^+ as well as the low energy ions, i.e., it can measure O^+ with a thermal energy range at which ions will return to the atmosphere due to the gravitational force once they flow upward. The TEX instrument observes during an isometric orbit from the Earth and is able to detect the short-term variation more easily than the IMAGE mission.

The key technology to clarify the above issues is to build bright optics in the spectral range of EUV. A multilayer coated mirror that has a high reflectivity in the EUV range is of particular importance [*Yoshikawa et al.*, 1997]. The capabilities of instruments with these technologies have been already demonstrated by the Planet-B mission [*Yoshikawa et al.*, 2001]. The success of the Planet-B experiment has motivated us to attempt continuous global EUV imaging.

3.3 Instruments

Effective imaging of the near-Earth plasma distribution requires global ‘snapshots’ with wide field-of-view (FOV). Lunar orbiter (SELENE) provides us with an ideal platform that commands a panoramic view of the near-Earth situation. The

telescope of EUV is mounted on a two-axis gimbal system together with Telescope of Visible light (TVIS), as shown in Figure 3.1. The pointing accuracies of the equatorial mounting are 3.24" around the Azimuthal and 2.68" around the Elevation axes. These correspond to the spatial resolution of 5 km on the Earth's surface.

The UPI-TEX imager is a type of normal-incidence telescope with a split thin metal filter, that is composed of aluminum/carbon (Al/C) and indium (In) in order to detect the resonance scattering emissions of helium ions (He II: 30.4 nm) and oxygen ions (O II: 83.4 nm). The primary scientific goals are: (1) to understand a global plasma distribution in the inner magnetosphere, and (2) to study the outflow mechanisms of oxygen ions from the polar ionosphere. The cold plasma in the plasmasphere also shows an active response at the high magnetic activity, which is contrary to a traditional understanding of plasmaspheric formation. Recent observations suggest that the heavy ions, such as oxygen ions, could also flow out. The remote sensing at O II by TEX gives us the first overall image of the world and will investigate the nature of the formation.

The optics in TEX consists of a multilayer-coated mirror to increase the reflectivity at 30.4 nm, a split metallic thin filter, and microchannel plates to pick up photon events (Figure 3.2). A high-voltage power supply (HVPS) is installed at one side, as shown in Figure 3.3, and a preamplifier unit is contained along the other side. Survival heaters for the main body of the instrument, the HVPS, and the preamplifier (not shown in Figure 3.3) are also installed. Table 3.1 summarizes the main features of TEX. The key points for the O II (83.4 nm) and He II (30.4 nm) imagings are (1) to eliminate the contamination from H I (Ly-α), which is emitted from the geocorona at a maximum intensity of 10 kR [*Rairden et al.*, 1986] and (2) to enhance the detection efficiency at 30.4 nm.

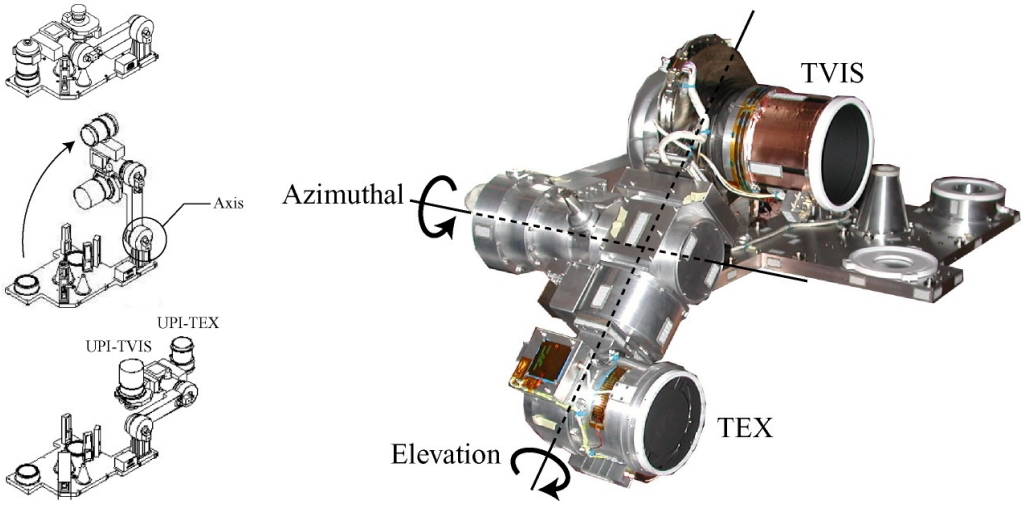

Figure 3.1: Upper atmosphere and Plasma Imager (UPI) onboard the SELENE satellite. Two telescopes are installed on the equatorial mounting (motor-controlled azimuthal and elevation axes) gimbal. After the insertion to the lunar orbit, the system is open (left panels) in order to make the two telescopes ready to point to the Earth. Pointing accuracy of the equatorial mounting is 3.24" around Azimuthal and 2.68" around Elevation axis.

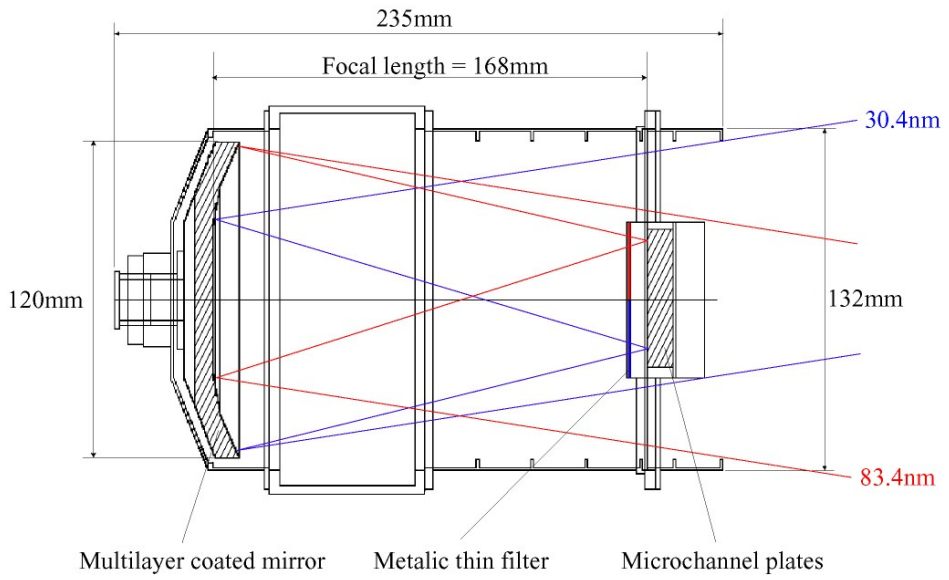

Figure 3.2: Configuration of Telescope of Extreme ultraviolet (TEX) onboard the SELENE satellite. Main optical components are a multilayer coated mirror, a split metal thin filter, and microchannel plates. Field-of-view is separate, O II (83.4nm, red line in the figure) and He II (30.4nm, blue line) areas.

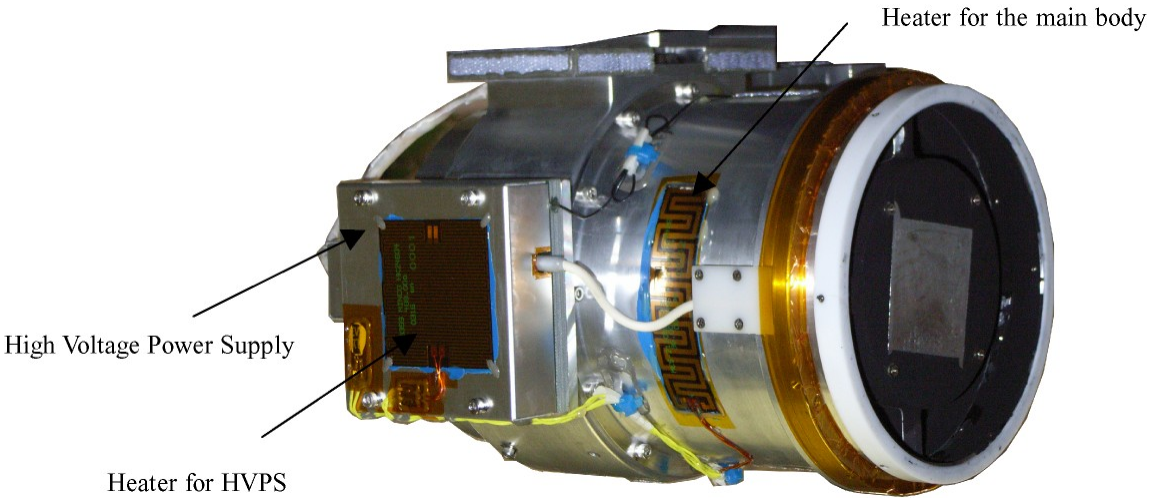

Figure 3.3: A photograph of TEX without a multilayer thermal insulator. A high-voltage power supply is installed at this side. The preamplifiers are put at the opposite side.

Table 3.1: Principal TEX design parameters

Prime focus	F/1.4	
Angular resolution	0.085 deg	
Spatial resolution	0.089 R_E	
Maximum time resoution	1 min	
Mass	2 kg	
Size	235 mm×φ140 mm	
Open Aperture	48.6 cm^2	
Format	128×128	
FOV	10.88×10.88 deg^2	
	Typ. (at 30.4 nm)	Typ. (at 83.4 nm)
Reflectivity of mirror	18.8%	20.2%
Transmittance of filter	11.2%	2.1%
Quantum efficiency of MCP	7.6%	9.8%
Sensitivity	0.014 cps/Rayleigh/bin	0.0036 cps/Rayleigh/bin

3.3.1 Mo/Si Multilayer Coated Mirror

In this section, I discuss the design and testing of a mirror coating. To realize a compact optics, a multilayer-coated mirror is designed for normal incidence reflection with a peak reflectivity at 30.4 nm, because most materials have much higher

single-layer reflectivities at 83.4 nm. For example, the normal incidence reflectance of silicon at 83.4 nm is about 37%. The mirror substrate is made of Zerodur, and the mirror has a focal length of 168 mm, a diameter of 120 mm, and a spherical shape to reduce aberration.

The recent study found that an Mg/SiC multilayer is a leading candidate for a highly reflective coating at 30.4 nm [*Yoshikawa et al.*, 2005]. Many samples were fabricated and tested to determine optical performance and degradation under conditions of vacuum and air. The Mg/SiC coating has a high reflectivity (>40%) at 30.4 nm, but the Mg/SiC stack is degraded even with only a short time exposure to the atmosphere [*Murakami et al.*, 2006]. Therefore, a conventional Mo/Si multilayer coating is used in this mission. This decision was supported by the results of some successful space-borne experiments in which the Mo/Si multilayers had been used [Yoshikawa et al., 1997, 2001]. For this space mission, 20 alternating Mo-Si layers (period of 16.49 nm, Mo thickness of 4.1 nm, Si thickness of 12.39 nm) on the Zerodur substrate of the mirror are chosen. All layers were deposited by ion-beam sputtering. The Nikon Company manufactured the substrate and coating of the mirror.

The calibration system consists of a windowless RF excited flow lamp filled with source gases and connected to a JOVIN YVON LHT30 30-cm scanning monochromator. Using an atomic source with the monochromator provides radiation limited only by the line widths of spectral lines from the light source. In the vacuum chamber, the mirror was set on a manipulator with three orthogonal axes of translation and a single axis of rotation aligned perpendicularly to the incident beam. The incident and reflected beams were detected by a photon detector. The reflectivity was determined by measuring the ratio of reflected and incident beams. This facility has a capability of measuring the reflectance (and transmittance) at any position as a function of wavelength and incident angle. This process was repeated several times for each wavelength to enable us to compensate for long-term drifts in the source intensity. Figure 3.4 shows the calibration system in the EUV facility.

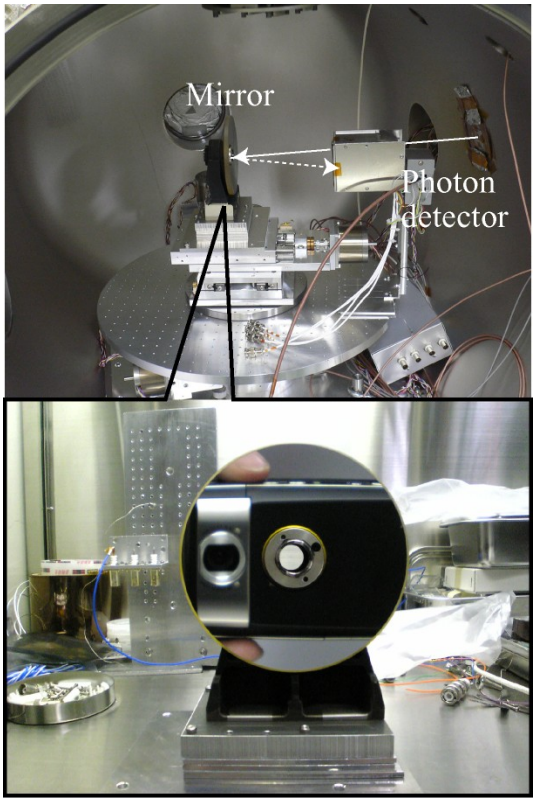

Figure 3.4: Calibration setup in the EUV facility. Flight mirror was set up as so-called "θ-2θ" configuration in order to measure reflectivity against incident angles, points, and wavelength.

Figure 3.5 gives the average reflectivity of the flight mirror as a function of wavelength. The reflectivities were measured at two points (30 and 50 mm from the center) toward every 90-degree radial direction using a 1-mm diameter beam. The line in the figure represents a theoretical curve of Mo/Si layers. At longer wavelengths, there is difference between the calculation and measurement, but this is due to the ambiguity of the optical parameter of Si in the EUV.

Figure 3.6 shows the dependence of the reflectivity on the incident angle to the mirror surface. In this case, the reflectivities were measured at three points (30, 40, and 50 mm from the center). The reflectivities at 30.4 nm have the maximum values (17.5-19.1%) at incident angles of 12-15 deg. This result indicates that the incident photons of 30.4-nm wavelength are pass through the surface and are reflected on the Mo/Si periodic multilayer structure. The difference of the angles exhibiting the maximum reflectivities in three points is mainly caused by the discrepancy of the thickness of the periodic multilayer coating. On the other hand, the reflectivities at 83.4

nm are slightly higher with larger incident angles and almost uniform at three points. This result indicates that 83.4-nm photons are reflected mostly on the mirror surface (i.e., oblique photons are reflected more efficiently) and the reflectivity does not depend on the thickness of the multilayer coating. The dependence on the incident angle and the reflectivities at different points on the mirror are taken into account when calculating the total sensitivity.

Although my testing of the mirrors shows that the Mo/Si multilayer coating was not particularly subject to degradation by oxidation, the coating was protected using normal procedures for handling. The mirror was stored in boxes purged by dry N2, and when the mirror had been installed in the telescope, the overall instrument was kept under as dry a N2 purge as practically possible.

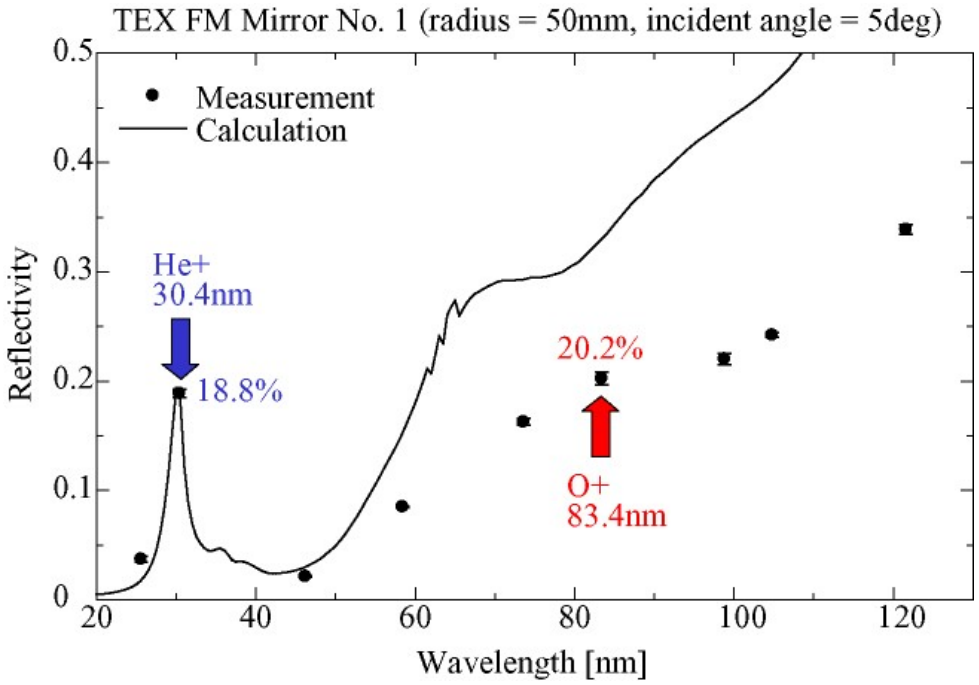

Figure 3.5: Reflectivity of a Mo/Si multilayer coated mirror used in TEX. The reflectivity achieved up to 18.8%. Unwanted longer wavelength emissions can be eliminated by a metallic thin filter.

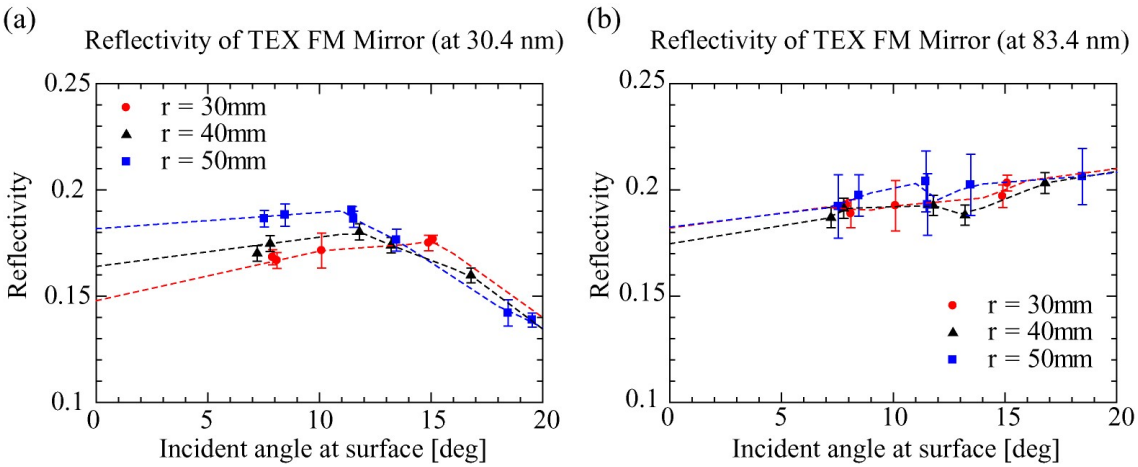

Figure 3.6: Dependency of the mirror reflectivity on incident angle to the mirror surface at wavelengths of (a) 30.4 nm and (b) 83.4 nm. The reflectivites were measured at positions of 30 mm, 40 mm, and 50 mm from the center.

3.3.2 Metallic Thin Filter

The filter material was chosen to provide high transmittance at the target wavelengths of 30.4 and 83.4 nm, while attenuating the unwanted Ly-α (121.6 nm) emission from the Earth's geocorona and the interplanetary medium. The filter is set at 12.3 mm off from the focal plane and is divided into two parts (Figure 3.7). One part has a carbon coating of 31.2 nm on an Al film (162.8 nm), which attenuates emissions whose wavelengths are longer than 40 nm; it allows the passage of He II (30.4 nm) with a small transmittance of He I (58.4 nm). The other part transmits O II (83.4 nm) and consists of a 292.9-nm thick layer of In. The filter is supported by a stainless steel mesh having a wire spacing of 0.36 mm and an open area of 75%. The Al material was permitted to oxidize in air on one side, and In was oxidized on both sides. The oxidized coatings stabilize the material and provide the additional benefit of reducing the transmission of Ly-α (121.6 nm).

Figure 3.7 (lower panels) compares the calibrated transmittances with theoretical ones. In the area of Al/C, carbon reduces transmittance at longer wavelengths, since Al itself has a fairly flat transmittance between 17 and 80 nm. Oxidizing, as noted above, reduces the transmittance over all wavelengths, especially at longer wavelengths. The difference between theoretical and calibrated curves indicates the oxidization of the Al face. I conclude that transmittance above 120 nm is below 10^{-9},

although no absolute calibrated value was available. The photon rejection at longer wavelengths is good enough to eliminate strong contamination from Earth's Ly-α geocorona. The In filter is used as band-pass filter to prevent He I, He II, and Ly-α emissions from contaminating O II emission. In particular, the Ly-α is so strong that the In filter is designed to be as thick as 292.9 nm despite low transmittance at 83.4 nm. The right panel of Figure 3.7 shows that the transmittance at Ly-α is 10^6-fold lower than that at 83.4 nm, but it is still sufficient to reduce the contamination of Ly-α.

The dependence on the incident angle of the filter is shown in Figure 3.8, together with the theoretical curves, showing good agreement with the theory.

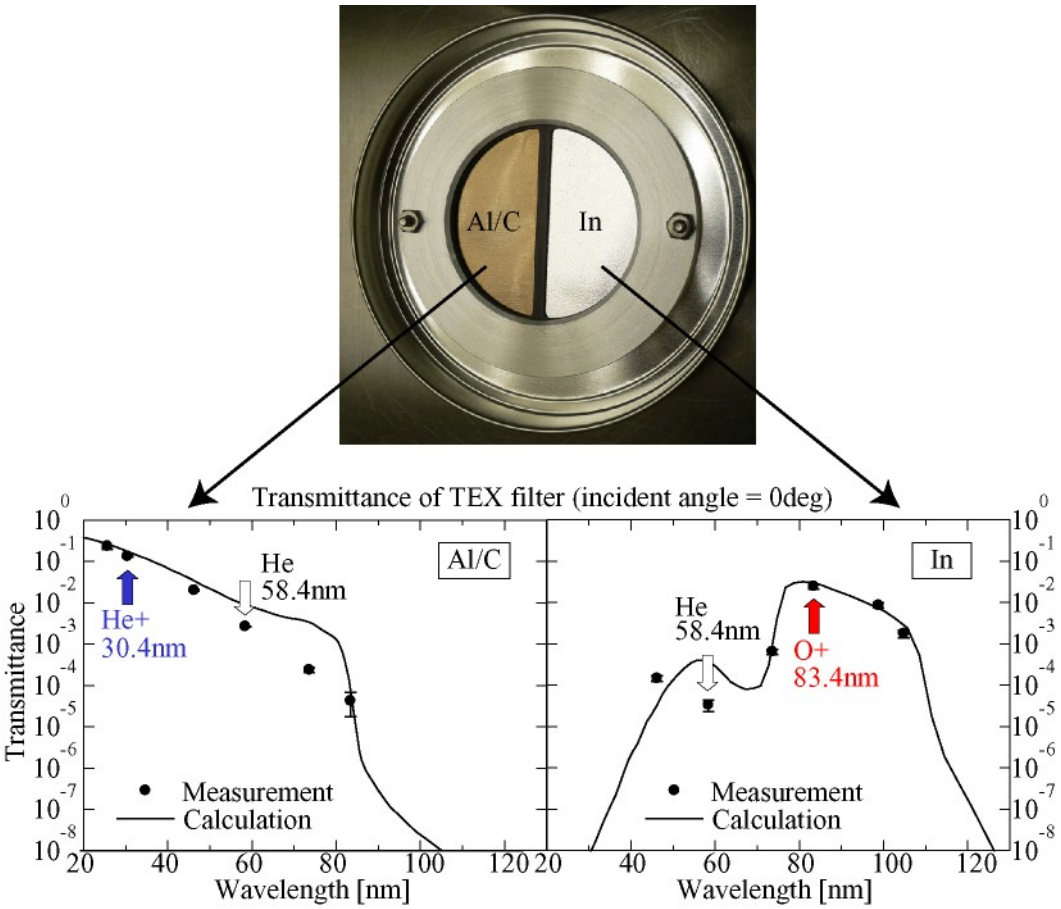

Figure 3.7: Transmittances of thin metallic filters. (Left) Aluminum (162.8 nm)/Carbon (31.2 nm) part. This part is used for He II (30.4 nm) transmittance. (Right) Indium (292.9 nm) used for O II (83.4 nm) transmittance.

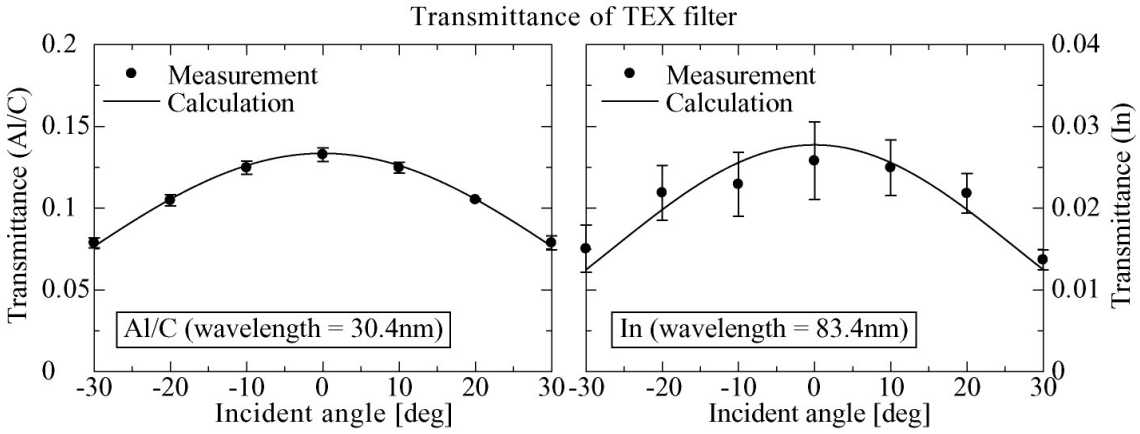

Figure 3.8: Dependency of filter transmittance on incident angle.

3.3.3 Microchannel Plates (MCPs) and Resistive Anode Encoder (RAE)

A three-stage MCP stack is used for photon detection. Each MCP has a circular shape with an active area of 13.9 cm^2, a bias angle of 8 deg, a 12-μm pore size, an L/D (a ratio of length to pore diameter) of 40:1 and a total resistance of 125 MOhm. Three MCPs were placed in direct contact as a back-to-back stack. An important indicator of the MCP stack performance is the pulse height distribution (PHD) of the single photon events. The gain and the PHD measurements were accomplished with a 30.4-nm illumination from the EUV lamp using the monochromator. Figure 3.9 shows the PHD with −2.3 kV and −2.5 kV applied at the MCP face. The pulse height ratio (PHR: width of the pulse height distribution) was somewhat broader—96% at -2.3 kV and 106% at -2.5 kV—than I would expect from a five-stage MCP stack. The dark count is 0.28 cps cm^{-2} at -2.3 kV and 0.37 cps cm^{-2} at -2.5 kV.

Figure 3.10 shows the dependence of the quantum efficiency (QE) on the incident angle to the channel axis, measured at wavelengths of 30.4 nm and 83.4 nm. The QEs at both wavelengths are lower with small incident angles. This corresponds to a situation where the photons strike the channel wall far from the MCP input, resulting in a number of events with low gains below the threshold of the low level discriminator.

Behind the MCPs, the resistive anode encoder (RAE) is placed to analyze the position of photon injection (Figure 3.11). The electron cloud emitted from the three-stage MCP consists of an order of 10^6 electrons and impinges on RAE. The electron cloud is divided over four electrodes at the corners in reverse proportional to the distance to them. Image distortion in the RAE arises mainly because the MCP

electron clouds at the edge run off the field. Therefore, an active area of 32×32 mm^2 on the RAE is used in order to avoid the distortion.

Figure 3.12 shows the block diagram of a position analysis in TEX electronics. The signal at each electrode is amplified by A-225 (AMPTEK). The pulse-shaper (A-206) further amplifies the signal and recognizes the event with a threshold level. When A-206 identifies a significant signal level, it sends a "ready" signal to the main electronics. PH300 holds the signal peak and ADC digitalizes the height of signal. The main electronics computes the position.

The image linearity and resolution were measured by imaging an array of pinholes in a metal mask illuminated by 30.4 nm beam, as shown in Figure 3.13. The ion-etching mask was placed at 8.3 mm off from the input face. The array consists of 0.5 mm or 1.0 mm holes with 5-mm distance. The pinhole mask image (left panel) clarifies none of distortion of the image within active area of 32-mm × 32-mm. Right panel is a cross-section of the left panel in the red line, indicates 250-μm resolution is achieved.

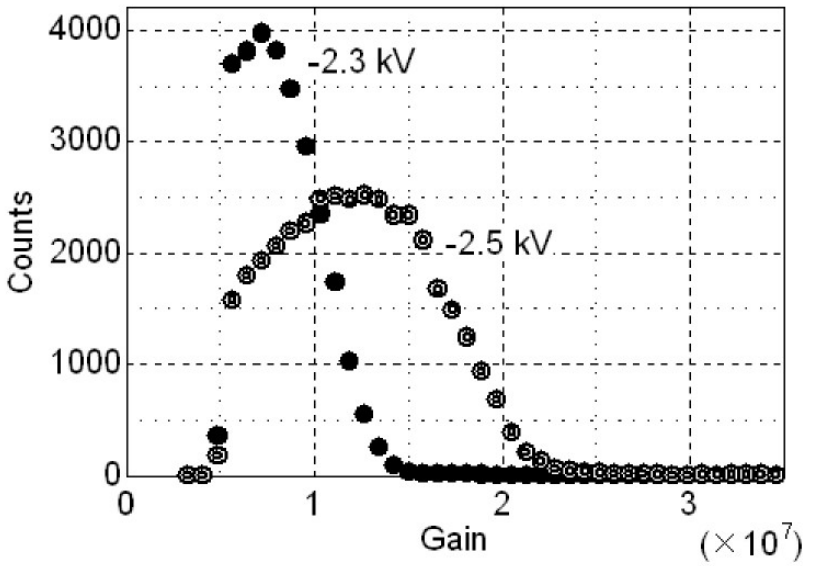

Figure 3.9: Pulse-height distribution of MCPs with -2.3kV and -2.5kV applied. Pulse-height-ratio (PHR) of 96-106% is achieved.

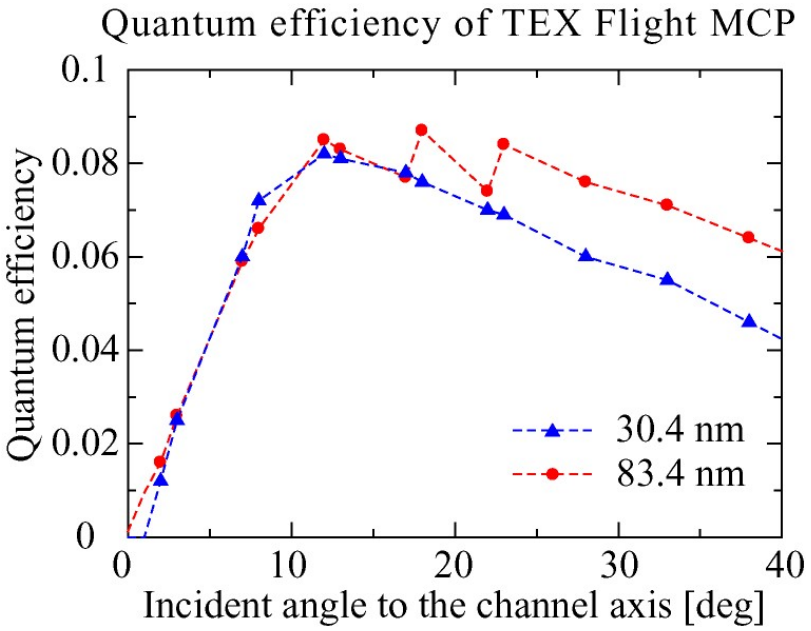

Figure 3.10: Dependency of the MCP quantum efficiency (QE) on incident angle to the channel axis. The QEs of both wavelengths are lower with small incident angles (<~10 deg). This corresponds to a situation where the photons strike the channel wall far from the MCP input, resulting in a number of events with low gains below the threshold of the low level discriminator.

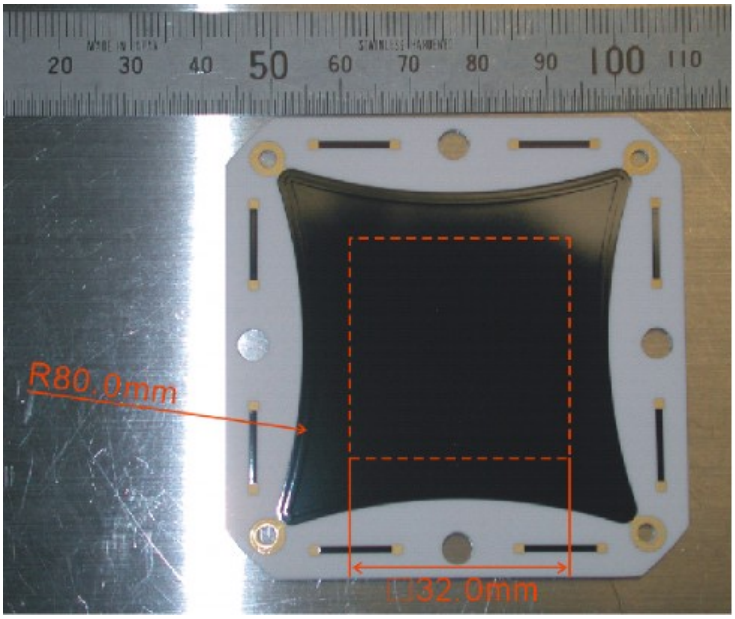

Figure 3.11: Photograph of Resistive Anode Encoder. Active area is 32 mm × 32mm. Resistive face is made of RuO_2. An active area of 32mm × 32mm at the center is used in order to avoid aberration near the edges.

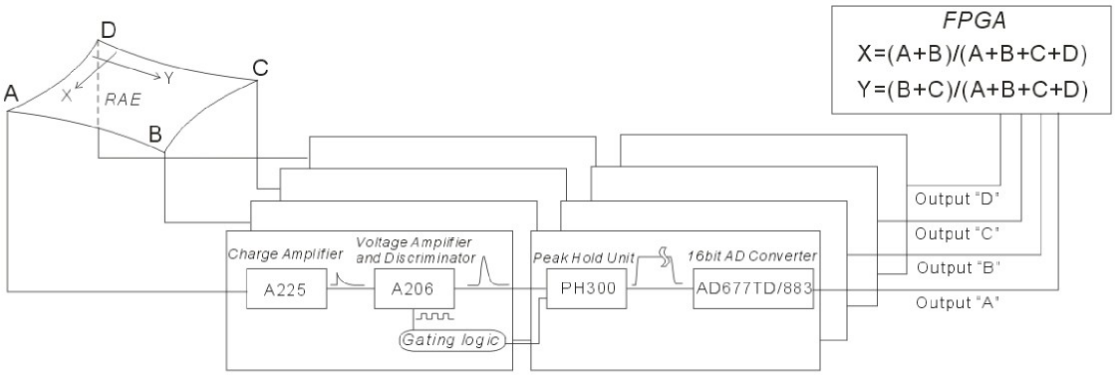

Figure 3.12: Block diagram of position analysis electronics. Preamplifiers, pulse-shapers with discriminators, and peak-hold ICs are all AMPTEK Co. products. This system realizes 128-bin (resolution) for each axis.

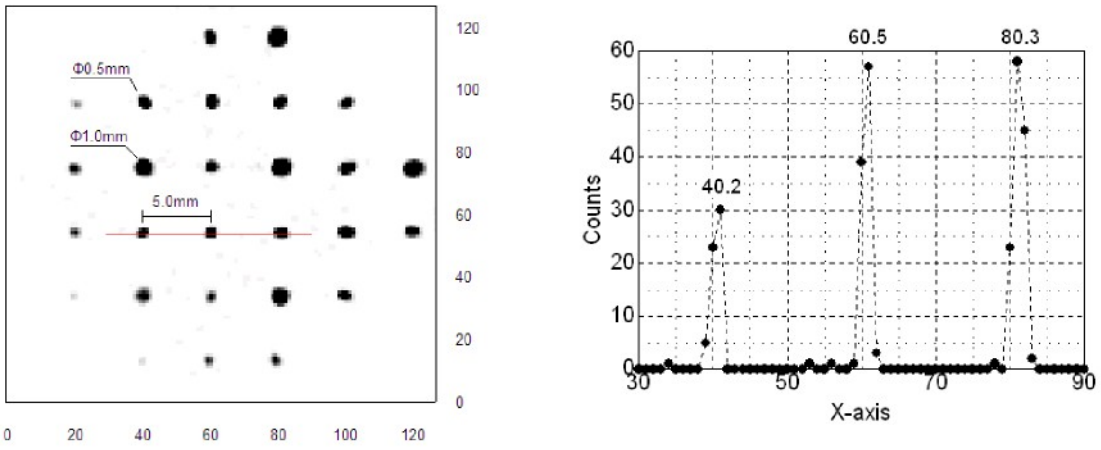

Figure 3.13: (Left) Pinhole mask image obtained by the TEX detector. I illuminated 30.4-nm beam onto the mask. Distance between holes is 5 mm and hole's diameters are 0.5 mm or 1.0 mm. (Right) Cross-section of red line in the left panel. Resolution of 32 mm/128 (250 μm) is achieved.

3.3.4 Electronics and High-Voltage Power Supply

SH-3 (Hitachi) controls the equatorial mounting gimbal system and the data interface to two telescopes as well as recognizes commands from command receiver. The high voltage power supply installed at the side of TEX is turned on by commands

from SH-3.

3.3.5 Total Sensitivity

The TEX imager has a full circular field-of-view (FOV) of 10.88 deg, and the 128×128 bins corresponding to the spatial resolution of 0.09 R_E on the Earth's surface from the lunar orbit. One-half of the FOV is used for O II (83.4 nm) detection; the other is for He II (30.4 nm).

The signal count rate N (cps) of the emission is represented by the following equations,

$$N = \frac{10^6}{4\pi} \times I \times S \times \Delta \times T_{\text{filter}} \times R_{\text{mirror}} \times E_{\text{MCP}} \quad \text{(cps)}, \tag{3.1}$$

where I is the brightness of emission in Rayleigh, S is an entrance aperture (cm^2), Δ is the sold angle of identical FOV, T_{filter} is the transmittance, R_{mirror} is the mirror's reflectivity, and E_{MCP} is a quantum efficiency of the MCP. The typical values of those instrumental parameters are summarized in Table 3.1. The telescope has a total efficiency of 0.014 cps/Rayleigh/bin for the He II (30.4 nm) and 0.0036 cps/Rayleigh/bin for the O II (83.4 nm).

Figure 3.14 shows the map of the total efficiency for all 128×128 bins on the detector, based on the laboratory photometric calibration. I constructed the map taking account of following points: (1) the flat field for a uniform light source calculated using the geometry of the telescope, and the dependences of (2) the mirror's reflectivity, (3) the filter's transmittance, and (4) the MCPs' QE on the incident angle. The map will be used to convert the signal count rate (cps) to intensity units (Rayleigh).

In the following, I estimate the signal-to-noise ratio (SNR) during the observation. The detector behaves as an ideal photon counter so that signal corresponds to the number of photon events collected during an exposure period (t_{exp}), and noise is the square root of signal.

Instrumental background (noise count from MCPs in the detector unit) is a primary noise source. The MCPs manufactured by Hamamatsu Photonics Co. had a noise count by 10.4 cps/cm^2 in the previous planetary mission, although the noise count in the laboratory was below 1 cps/cm^2 [*Yoshikawa et al.*, 2000a; *Yamazaki et al.*, 2006]. This increase was due to cosmic ray and/or high-energy particle bombardments in the magnetosphere. For the lunar environment, I assume the latter component is negligible

but as the worst case analysis, I assume 10.4 cps/cm^2 (0.0065 cps/bin) as dark count in lunar orbiter.

The second noise source is a contamination from He I (58.4 nm) and Ly-α emissions. As stated above, Ly-α is sufficiently reduced by the metallic filter on both sides. The intensity of Ly-α is insensitive to my estimation of SNR. In the following discussion, I assumed and fixed the Ly-α intensity at 5 kR. Another possible contamination is He I (58.4 nm) emission. This is fairly well reduced by the filter, but it has the potential to contaminate the observation. The maximum geocoronal He I (58.4 nm) intensity and the interstellar He I (58.4 nm) intensity are assumed to be 500 Rayleigh [Meier, 1991] and 10 Rayleigh [Yamazaki et al., 2002], respectively.

During the measurement, a detector pixel sees the EUV signal (N_{signal}), measured in cps/bin, and the background ($N_{\text{background}}$: instrumental background plus contaminations from the other EUV emissions), measured in the same units. The number of signal counts is the total observed counts minus the background as follows:

$$N_{\text{signal}} = N_{\text{total}} - N_{\text{background}}$$

$$\sigma_{\text{signal}} = \sqrt{\sigma_{\text{total}}^2 + \sigma_{\text{background}}^2} \approx \sqrt{\sigma_{\text{signal}}^2 + 2\sigma_{\text{background}}^2}$$

$$\approx \sqrt{N_{\text{signal}} + 2N_{\text{background}}} \tag{3.2}$$

$$SNR = \frac{N_{\text{signal}}}{\sigma_{\text{signal}}} = \frac{N_{\text{signal}}}{\sqrt{N_{\text{signal}} + 2N_{\text{background}}}}.$$

Figure 3.15 shows SNRs based on the above assumptions. Expected intensities discussed in Section 3.2 are also indicated. Here “SNR=2 or 3” is set as a norm. For He II (30.4 nm) observation, the observation mode (2-min exposure and 0.09 R_E resolution) is able to identify the main body of the plasmasphere with a high reliability (SNR=3). The identifications of plasmapause and refilling region in the trough discussed in Section 3.2 are feasible with a fairly good SNR. Imaging polar wind by O II (83.4 nm) is a challenging target, but the 30-min exposure with 0.5 R_E resolution allows the polar wind to be visible with SNR=2.

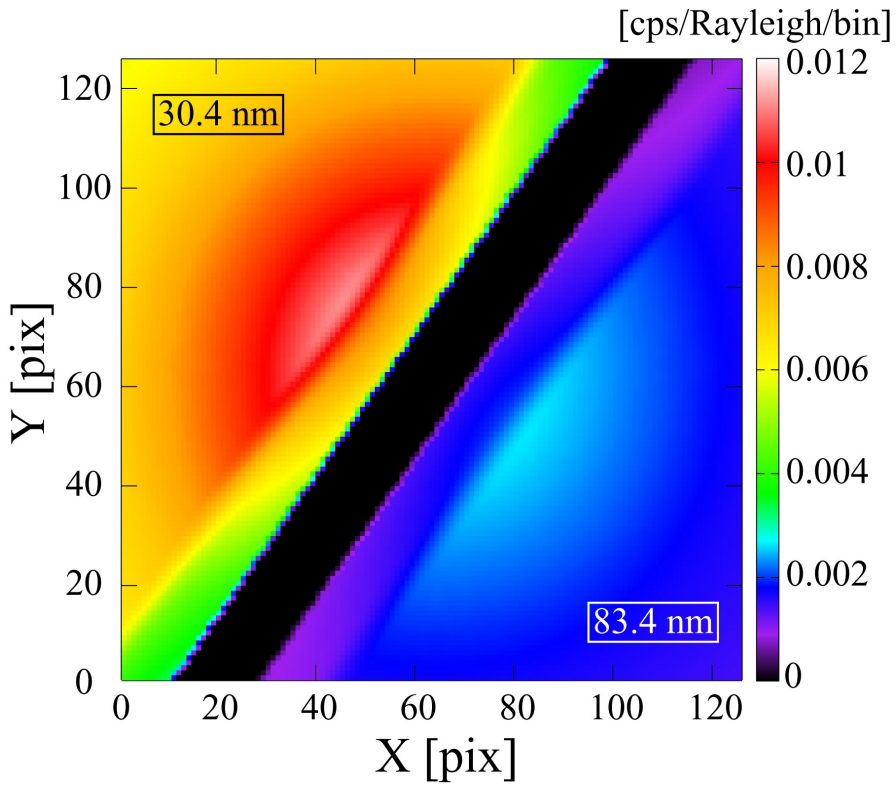

Figure 3.14: The map of the total efficiency of TEX for all 128×128 bins, based on the laboratory photometric calibration. The map is divided into two areas: the sensitivity for He II (30.4 nm) is represented in the upper left and that for O II (83.4 nm) is represented in the lower right, respectively. The bins where the photons of both wavelengths arrive are shown as a black region.

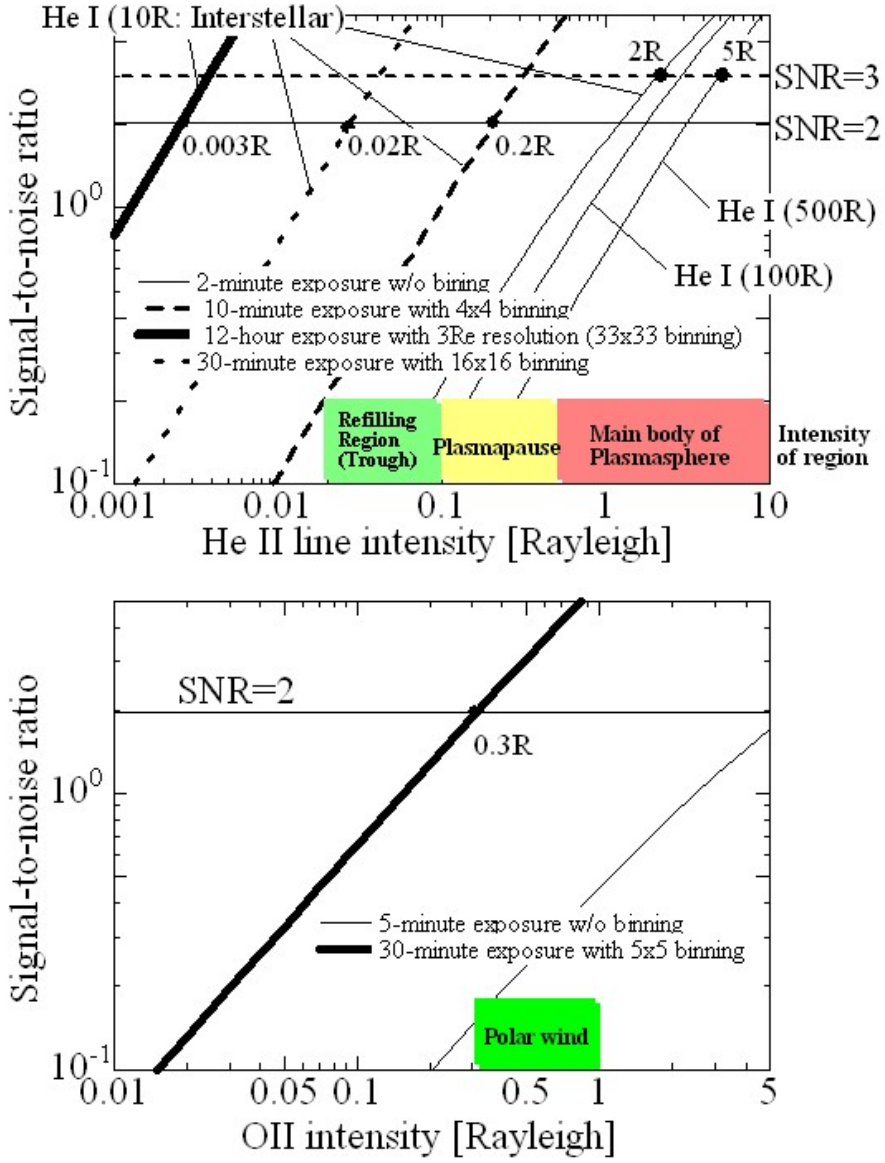

Figure 3.15: (Upper panel) Expected Signal-to-Noise Ratios for He II (30.4 nm) observation. The SNR is insensitive to ionospheric contamination at 121.6 nm. Here Ly-alpha intensity is assumed to be 5kR. The intensity of He I (58.4 nm) is assumed to be 500R, 100R (ionosphere) and 10R(interstellar) as indicated. (Lower panel) Expected SNR for O II (83.4 nm) observation. The observation is free of ionospheric He I and Ly-alpha contaminations in the range of 10-500R for He I (58.4 nm) and 1k-30kR for Ly-alpha. In this plot, the intensities of He I and Ly-alpha are 100R and 5kR, respectively.

3.4 Summary

The UPI-TEX instrument onboard the SELENE satellite will image near-Earth cold plasmas at O II (83.4 nm) and He II (30.4 nm) emissions. The UPI-TEX instrument has enough performance to detect the oxygen ion outflow, the transport route from the polar ionosphere into the magnetosphere, and the plasmasphere. The 2-D O II imagery is expected to identify the transport routes and mechanisms of the cold O^+ ions and to reveal a quantitative balance between the supply and loss, including thermal plasma. On the other hand, the detection of He II (30.4 nm) by the TEX instrument is devoted to contributing to conventional plasmasphere physics.

4 Development of High-resolution Imaging Detector using Five Microchannel Plates and a Resistive Anode Encoder

4.1 Introduction

Microchannel plates (MCPs) are widely used to detect ions, electrons, and photons in laboratory and space applications. One of the position sensitive anodes for MCPs is a resistive anode encoder (RAE) [*Lampton and Carlson*, 1979]. In the position sensitive detector with an RAE, the ratio of the charge signals delivered at its four corners or edges depends only on the *X* and *Y* centroid location of the event, and so the X-Y coordinates of each event can be determined in essentially real time with a pair of ratio circuits fed by these signals. The simplicity both in the anode itself and in the associated electronics has led to the resistive anode becoming one of the most popular readout methods for photon counting systems.

In a resistive anode position-sensitive system, the spatial resolution depends on the signal-to-noise ratio (SNR) at the anode terminals and therefore depends on the MCP gain. Here, "signal" refers to the charge produced by a single photoelectron, and is synonymous with the gain of the electron multiplier structure. The "noise" is mainly caused by the extraneous electrical noise introduced into the position analyzing system and the thermally generated noise. The double (so called "Chevron" or "V-stack") or triple ("Z-stack") MCPs are commonly used as a method of obtaining a high gain ($>10^6$). Ideally the output pulses should be all the same amplitude for good pulse counting. An MCP stack, however, does not give a certain value of the gain for every photoelectron event. The statistical variation of the gain of a V-stack or a Z-stack MCP is generally characterized by the pulse height distribution (PHD) with typical values of FWHM of about 80-120%. Therefore, it is desirable that the MCP stack exhibits a high and stable gain with a narrow PHD.

The position-sensitive detectors using an RAE and a usual V-stack or Z-stack MCP typically give spatial resolutions of the order of 100×100 to 250×250 pixels. *Lampton and Carlson* [1979] reported that their sample detector consisting of two MCPs in a V-stack configuration and an RAE achieved the resolution of 100×100 pixels. Recently, the detector using a Z-stack MCP and an RAE was mounted in the Telescope of Extreme Ultraviolet (TEX) onboard the SELENE satellite. The detector had an active area of 32×32 mm and it achieved the 250-μm resolution, corresponding to the format

of 128×128 pixels [*Yoshikawa et al.*, 2008] (see Chapter 3).

This degree of the spatial resolution has proven satisfactory for a number of applications in laboratory and space flight photon counting, but the space science community needs a higher-resolution imaging detector to be applied on the optics for the future missions. For example, a UV spectrometer in the Mercury mission needs an MCP detector with a spatial resolution of 512×512 pixels in order to pick up small atmospheric signals around Mercury with a high wavelength resolution.

One of the techniques to improve the spatial resolution of the detector with an RAE is using five MCPs in a set of V-stack and Z-stack [*Firmani et al.*, 1982; *Floryan and Johnson*, 1989]. *Firmani et al.* [1982] and *Floryan and Johnson* [1989] investigated the performance of the similar type of detector incorporating five MCPs arranged in a set of V- and Z-stacks with an inter-stack gap (a V-Z gap). They each measured the spatial resolution of their own detector under a wide variety of applied potentials, and found that a negative potential applied across the V-Z gap enabled the detector to achieve the spatial resolution of the order of 500×500 pixels. It was not completely understood, however, why applying the negative potential across the V-Z gap improved the spatial resolution. *Firmani et al.* [1982] suggested that applying the negative potential expanded the electron cloud arriving at the Z-stack and a high stable gain was achieved due to a large number of excited channels. On the contrary, *Floryan and Johnson* [1989] suggested as follows: (1) electrons with sufficiently high energies to reach the Z-stack were emitted far enough up the channels in the V-stack and highly collimated by the channels, (2) the number of excited channels at the Z-stack was reduced, and (3) the Z-stack MCP was completely operated in the saturated mode to exhibit a narrow PHD.

It is necessary to understand the effect of the negative potential applied across the V-Z gap on the electron distribution at the Z-stack input, in order to use this technique for other applications and to reduce the effort at experimental measurements for optimization purposes. Computer simulation gives us useful information on the distribution of the electron cloud from the MCP output [*Timothy and Bybee*, 1975; *Tremsin and Siegmund*, 1999; *Saito et al.*, 2007]. *Zanodvorov et al.* [1980] presented a "ballistic" model of the charge cloud propagation based on the differential electron distributions at the MCP output, which had been measured in the experiments of *Bronshteyn et al.* [1979]. In this approach, no interactions between the electrons in the

cloud are taken into account, i.e., the electric field is assumed to be constant rather than self-consistent.

In this study, I use a similar ballistic approach for calculating the distribution of the electron cloud across the V-Z gap. The result gives us important information on the effect of the negative potential across the V-Z gap. Then, to confirm the result of the calculation, experiments are described to investigate the dependency of the spatial resolutions and the PHDs on the applied negative potential. This work has a direct impact on the way in which MCPs can be optimized to satisfy future mission requirements on the spatial resolution, and enhances the capabilities for the mission performance.

4.2 Calculation

The statistical nature of the electron avalanche, originating at the output of the MCP channels, inhibits a precise calculation of the charge cloud evolution. The angles and velocities of the output electrons exhibit large variations depending not only on the MCP intrinsic parameters (such as the length-to-diameter ratio L/D, the secondary electron emission coefficient of the semi-conductive layer, the end spoiling, etc.), but also on the mode and sometimes even the history of operation. However, below I suggest some approximation which enables me to simulate the electron cloud development in the gap between the V- and Z-stacks (V-Z gap) and obtain some information on the size of the electron cloud at the input surface of the Z-stack MCP.

Following the same approach as the past studies [*Zanodvorov et al.*, 1980; *Tremsin and Siegmund*, 1999], the trajectories of all electrons in the cloud are assumed to be purely ballistic, and the differential distribution function at the output of the MCP, measured by Bronshteyn et al. [1979], is used. For simplicity, it is assumed further that (1) the original size of the charge cloud at the V-stack output, determined by the number of excited channels (~6.5 channels [*Wiza et al.*, 1977; *Tournianski et al.*, 2004]), is negligible, that (2) no interactions occur between the electrons in the cloud, and that (3) the bias angle of the output MCP is 0 deg and then the electron distribution is symmetric to the channel axis. Figure 4.1 shows the coordinate system for my model. Using the electron distribution function, it is possible to calculate the ballistic trajectories of all electrons and to estimate the spatial distribution of the cloud at any distance from the MCP output.

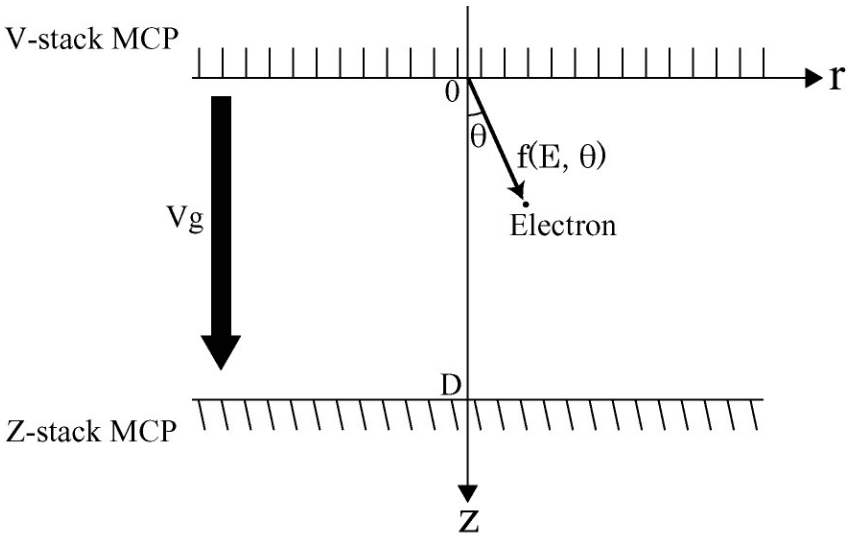

Figure 4.1: Schematic diagram of the coordinate system used for the calculation of the charge cloud spreading. Potentials accelerating electrons from the V-stack toward the Z-stack are considered positive.

I use one of the experimental distributions of *Bronshteyn et al.* [1979], which was measured using a single MCP with an L/D of 60:1, 20-μm channels, and an applied voltage of 1.4 kV. The electron distribution function at the MCP output can be approximated by the following function [*Zanodvorov et al.*, 1980]:

$$f(E,\theta) = e^{-\tau^2/2\Delta^2}\left|A(\tau)e^{-(E-E_0)^2/2\sigma_0^2} - B(\tau)e^{-(E-E_1(\tau))^2/2\sigma_1^2(\tau)}\right|, \tag{4.1}$$

where E and θ are the electron output energy and angle, respectively, and $\tau = \tan\theta$. The unknown parameters in this distribution were chosen to fit the experimental data [Bronshteyn et al., 1979] as follows:

$$\begin{aligned} &E_0 = 3 \text{ eV}, \sigma_0 = 12 \text{ eV}, \Delta = 0.2, \\ &A(\tau) = 50.398e^{7.3822\tau}, B(\tau) = 25.992e^{9.8642\tau}, \\ &E_1(\tau) = 314.45e^{-6.9515\tau}, \sigma_1(\tau) = 147.62e^{-9.7077\tau}. \end{aligned} \tag{4.2}$$

Figure 4.2 shows the distribution function $f(E, \theta)$ at various constant values of θ. The equation of motion of an electron in the cloud at the moment t can be written as,

$$r = \sqrt{\frac{2E}{m_e}}t\sin\theta, \tag{4.3}$$

$$z = \sqrt{\frac{2E}{m_e}}t\cos\theta + \frac{q_e V_g t^2}{2m_e D}, \tag{4.4}$$

where r is the radial distance from the channel axis, z is the distance from the V-stack output, D is the distance between the V- and Z-stacks, V_g is the accelerating bias in the V-Z gap, and q_e and m_e are the electron charge and mass, respectively. In this work, potentials accelerating electrons from the V-stack toward the Z-stack are considered positive. Using Eq. (4.3) and (4.4), I obtain the radial distance r_0 at the Z-stack input ($z = D$).

Using the electron distribution function (4.1) (summarized in Figure 4.2), I calculated r_0 of all electrons and estimated the cloud spatial distribution at the input surface of the Z-stack with various values of V_g. The radial distributions of electrons, arriving at the Z-stack input with sufficient energy to excite secondary electrons (> 10 eV [*Martin and Bowyer*, 1982; *Siegmund et al.*, 1988]), are calculated with the parameters of D = 2.5 mm and V_g = 0, -100, and -200 V. Figure 4.3 shows the result. In Figure 4.3, the total number of electrons arriving at the Z-stack for each V_g is normalized. Applying the negative inter-stack potential clearly reduced the size of the electron cloud. This means that the outer component of the electron cloud consisting of the low energy electrons emitted at large angles (as shown in Figure 4.2) is mainly eliminated. Therefore, the result of the calculation indicates that the negative inter-stack potential allows the Z-stack MCP to be operated in the completely saturated mode and a narrow PHD will be achieved, as suggested by *Floryan and Johnson* [1989].

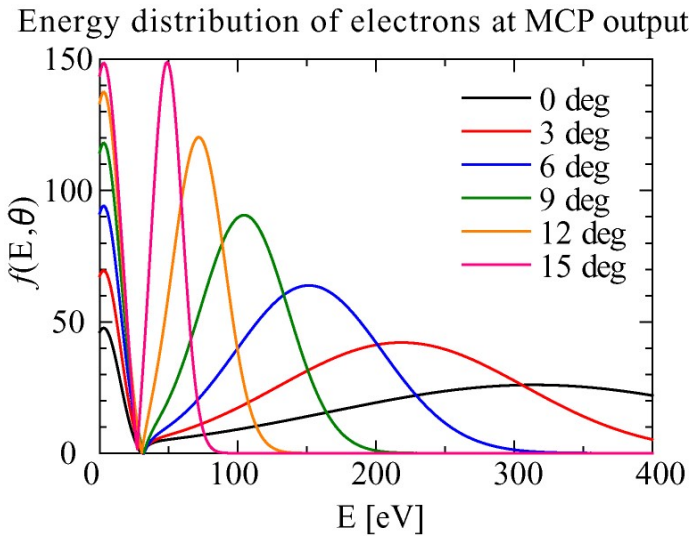

Figure 4.2: Energy distribution curves of electrons at MCP output at fixed output angles, measured by Bronshteyn et al. [1979]. The electrons with high energy are concentrated in small output angles.

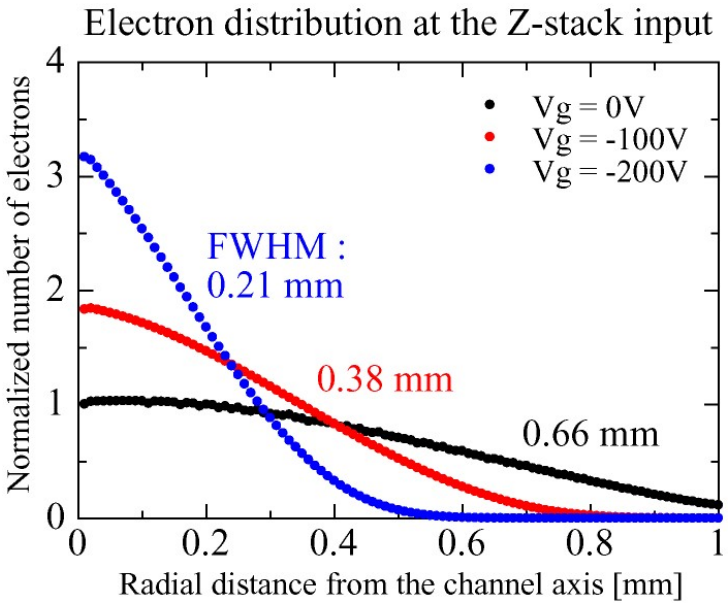

Figure 4.3: The distribution of the electron cloud at the Z-stack input calculated with the ballistic model. The total number of electrons arriving at the Z-stack for each *V*g is normalized. Applying the negative inter-stack potential clearly reduced the size of the electron cloud, from the FWHM of 0.66 mm to 0.21 mm.

4.3 Measurement

The experimental approach was also performed to check whether the result from the calculation is realistic. The prototype detector used in the measurements consists of an input window made of synthetic silica, a Cs_2Te photocathode, five MCPs in a set of V- and Z-stacks, and an RAE. The photograph and the schematic geometry of the detector are shown in Figure 4.4 and Figure 4.5, respectively. The photocathode converts the incoming photons into photoelectrons. The photoelectron is accelerated towards the MCP in the cathode gap. The photoelectrons impact the walls of the MCP channels causing a charge avalanche, giving an overall charge multiplication of $\sim 2\times10^7$. This charge cloud is drifted from the MCP output to the RAE, and its centroid position can be determined. The four output charge signals from the RAE are amplified and shaped by four preamplifiers. The discriminator discards signals which are too small to be properly processed and signals resulting from simultaneous or near-simultaneous events on the RAE. For valid signals, the centroid position of the electron cloud is calculated by measuring the peak voltage of the pre-amplifiers for each corner A, B, C,

and D of the RAE. The following algorithm is then used to obtain its position in the X-Y coordinates:

$$X = \frac{A + B}{A + B + C + D}, \tag{4.5}$$

$$Y = \frac{B + C}{A + B + C + D}. \tag{4.6}$$

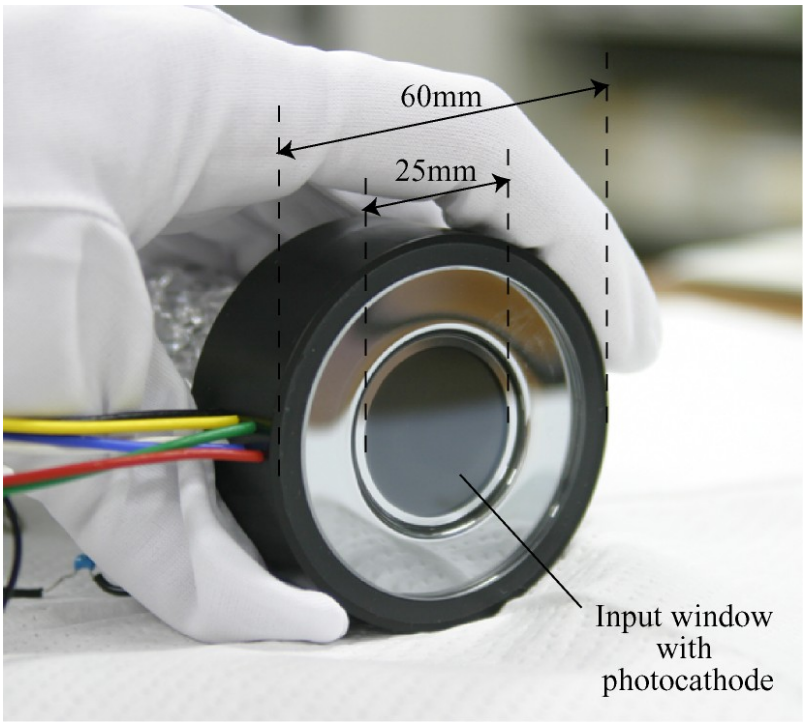

Figure 4.4: A photograph of the prototype detector. The detector head consists of an input window, a photocathode, five MCPs in a set of V- and Z-stacks, and a resistive anode. Inside the input window, the components are sealed in vacuum. The diameter of the active area is 25 mm.

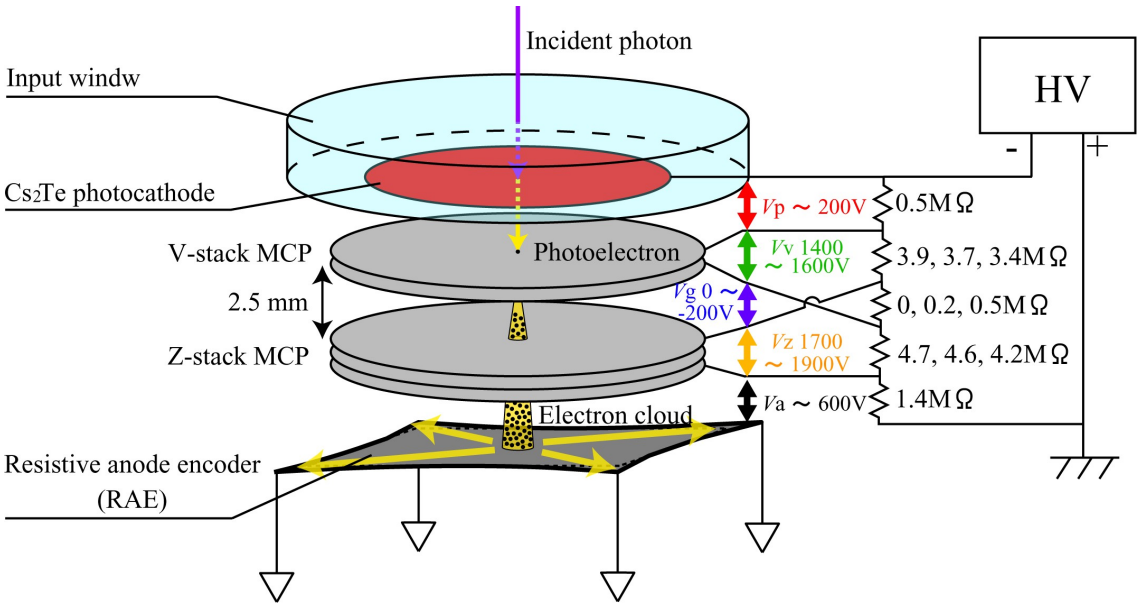

Figure 4.5: A schematic diagram of the prototype detector. The detector requires five separate potentials to operate: the potential between the photocathode and the input surface of the V-stack (V_p), that across the V-stack (V_v), that between the output surface of the V-stack and the input surface of the Z-stack (V_g), that across the Z-stack (V_z), and that between the output surface of the Z-stack and the resistive anode (V_a).

The MCPs incorporated in the detector is arranged in a set of V-stack (two plates) and Z-stack (three plates) with a gap of 2.5mm, as shown in Figure 4.5. Each MCP has a circular shape with an active diameter of 25 mm, a bias angle of 12 deg, a 10-μm channel diameter, and an L/D (a ratio of length to channel diameter) of 40:1. The resistances of the V-stack and the Z-stack are ~90 MΩ and ~120 MΩ, respectively. The RAE has an active area of 23×23 mm^2. In this measurement, however, I use a circular active area of 16-mm diameter defined by an aperture mask placed in contact with the output surface of the Z-stack to avoid the distortion. The detector requires five separate potentials applied as shown in Figure 4.5: the potential between the photocathode and the input surface of the V-stack (V_p), that across the V-stack (V_v), that between the output surface of the V-stack and the input surface of the Z-stack (V_g), that across the Z-stack (V_z), and that between the output surface of the Z-stack and the resistive anode (V_a). It is possible to operate the detector with a wide variety of combinations of these five potentials. In this work, potentials which accelerate electrons from the

photocathode toward the anode are considered positive, and those which decelerate electrons in this direction are considered negative. The applied voltages of V_p and V_a were constantly ~200V and ~500V, respectively, for all the measurements.

I measured the spatial resolution of the detector using the USAF 1951 resolution test target. My experimental setup is shown schematically in Figure 4.6. The light for all tests was 633 nm light produced by an intensity-stabilized laser. The test target was illuminated uniformly through diffusers, and the image of the test pattern was projected onto the photocathode by a relay lens. Optical focus of the test-pattern image on the photocathode was obtained by taking a series of spatial resolution measurements (described below) at various distances between the relay lens and the detector, and by determining the position where the maximum resolution was achieved. Figure 4.7 shows a typical image of the test target and a cross-sectional histogram at 6.3 lp/mm across it, obtained with V_v of 1420V, V_g of 0V, and V_z of 1710V applied. The contrast was calculated from the images of the test target with a simple formula, (Max – Min) / (Max + Min). Analyzing the profiles of the test-pattern images allows the resolution of the detector to be determined.

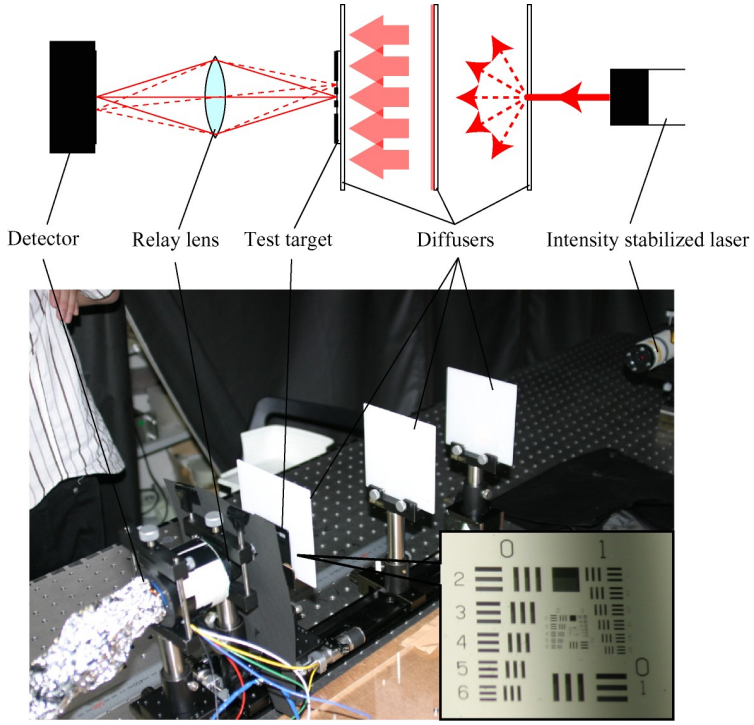

Figure 4.6: A schematic diagram (upper) and a photograph (lower) of the setup of the measurement. The test target is illuminated uniformly. The relay lens transmits the image of the test target to the photocathode of the detector.

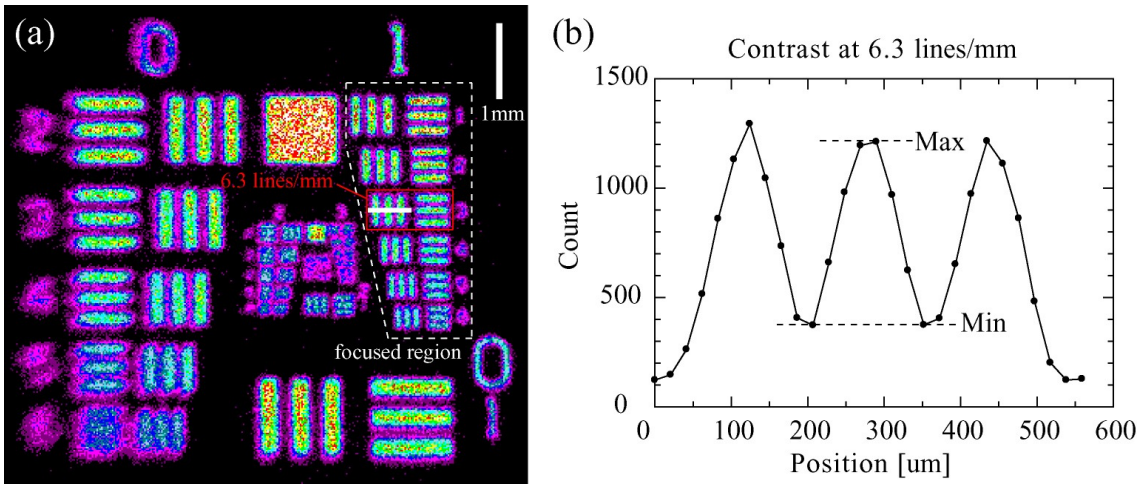

Figure 4.7: (a) A test target image obtained by the experimental detector. The series of patterns encircled by dotted line are well focused. (b) A cross section profile of (a) taken along the white line at 6.3 lines/mm. The contrast at 6.3 lines/mm is 0.53.

In this work, I recorded a number of test target images and pulse height distributions obtained with different combinations of applied potentials. I investigated the relationship between the negative inter-stack potential, the spatial resolution, and the pulse height distribution with the experimental approach.

4.4 Results and Discussion

In the first measurement, the dependence of the spatial resolution on the gain and the PHD was examined. I measured the PHDs and spatial resolutions with various potentials applied, and the results are shown in Figure 4.8. Each applied potential is also displayed. As seen in Figure 4.8a, the peak gain increases and the distribution becomes wider as the applied potential increases. In Figure 4.8b, while the contrast linearly increases with the gain below 1.6×10^7, there is no correlation between the contrast and the gain above 1.6×10^7. This result means that the spatial resolution mainly depends on the number of events with low gains ($< \sim0.4\times10^7$ in this measurement) which have the low SNR. In this measurement, therefore, it was confirmed that the spatial resolution of the detector surely depends on the gain and the PHD of the MCPs.

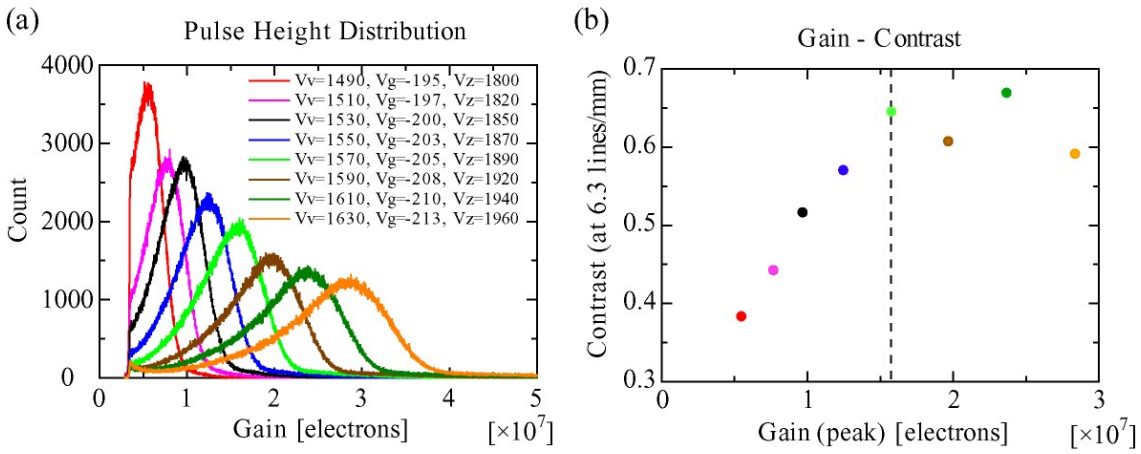

Figure 4.8: (a) Pulse height distributions (PHDs) with various high-voltage applied. The gain increases and the distribution becomes wider as applied voltage increases. (b) Dependence of the contrast at 6.3 lines/mm on the gain. The PHD corresponding to each point is shown in (a) in the same color. While the contrast linearly increases with the gain below 1.6×10^7, there seems to be no correlation between the contrast and the gain over 1.6×10^7.

In the second measurement, the effect of the negative inter-stack potential (V_g) on the PHD was examined. Figure 4.9 shows the PHDs with V_g of 0V, -76V, and –205V applied. The applied potentials across the V-stack (V_v) and across the Z-stack (V_z) are controlled appropriately so that each PHD has approximately the same gain at the peak. The PHD clearly got narrower as V_g increased. The full width at half maximum (FWHM) of the PHD (PHR: pulse height ratio) was excellently improved from 165% (V_g = 0V) to 38% (V_g = –205V). This narrowing of the PHD introduced by applying the negative inter-stack potential is consistent with the prediction from my calculation (described in Section 4.2).

Finally, the dependence of the spatial resolution on V_g was examined. Figure 4.10 shows modulation transfer functions with V_g of 0V, -76V, and –205V applied. The spatial frequencies where the contrasts equal to 0.33 are also displayed. Applying the negative inter-stack potential improved the spatial resolution by ~14%. This result is consistent with that obtained in the second measurement. In Figure 4.10, furthermore, there seems to be no difference between the spatial resolutions with V_g of –76V and –205V. This characteristic can be explained by the result of the first measurement, i.e. nearly the same numbers of events with low gains below $\sim0.4\times10^7$ were achieved. As a

result, the spatial resolution of 54 μm, corresponding to 400×400 pixels in my detector, was achieved by using V- and Z-stacks and applying the negative inter-stack potential.

The achieved resolution is lower than that of the order of 500×500 pixels reported by *Firmani et al.* [1982] and *Floryan and Johnson* [1989]. This difference would mainly result from the deficiency of optimizing the potentials applied between the photocathode and the V-stack input (V_p) and between the Z-stack output and the RAE (V_a). *Floryan and Johnson* [1989] reported that the resolution depends on V_a and especially on V_p. They achieved the highest resolution of 500×500 pixels with V_p of 700V, while it was 200V in my measurement. It is necessary to measure the spatial resolution of the detector with higher V_p for the future missions. Nevertheless, this study revealed the effect of the negative potential applied across the inter-stack gap on the distribution of the electron cloud, the PHD, and the spatial resolution by the calculation and the experiments. Using the same technique I can optimize the characteristics of the position sensitive detectors incorporating an RAE to the future missions.

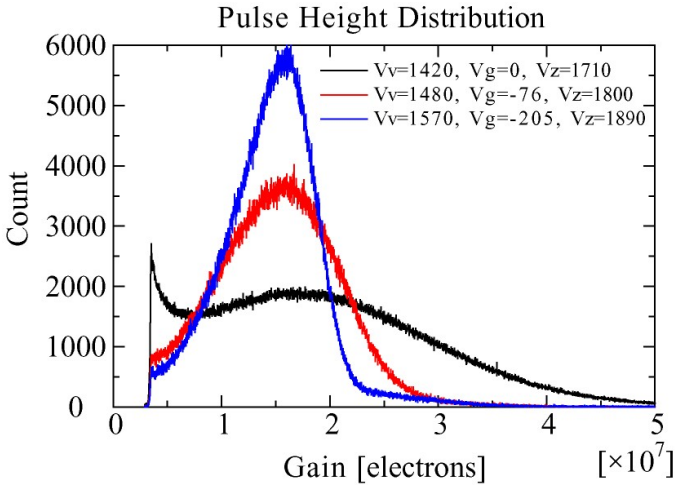

Figure 4.9: Dependency of the pulse height distribution on the potential between the output surface of the V-stack and the input surface of the Z-stack (V_g). The distribution becomes sharper as V_g increases. The applied potentials across the V-stack (V_v) and across the Z-stack (V_z) are controlled appropriately so that each PHD has approximately the same gain at the peak.

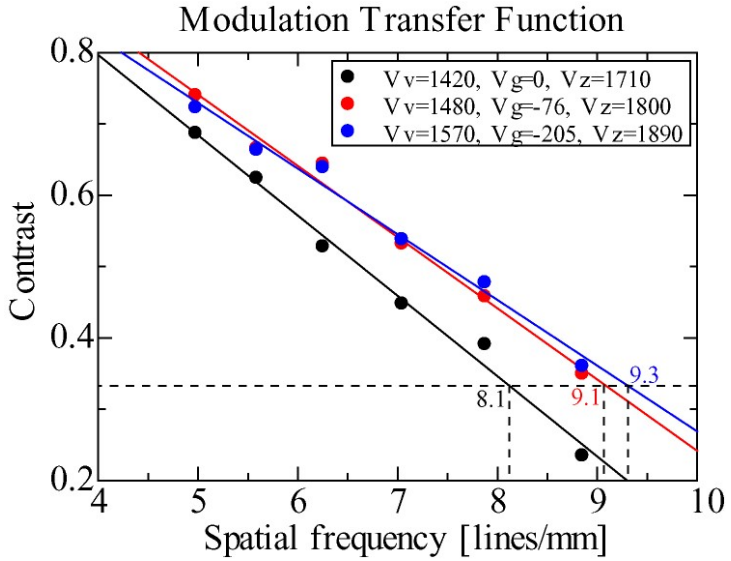

Figure 4.10: Dependency of modulation transfer function (MTF) on V_g. The PHD with each V_g applied is shown in Figure 4.9 in the same color. Applying negative V_g increases the spatial resolution by ~14%. There seems to be no difference between the spatial resolutions with V_g of –76V and –205V.

4.5 Summary

I have investigated the effect of the negative potential applied across the inter-stack (V-Z) gap on the PHD and the spatial resolution by means of calculation and experiments. The calculation with a simple ballistic model showed that the negative inter-stack potential (V_g) reduced the size of the electron cloud by ~70%. The result suggests that under such a condition the Z-stack MCP is operated in the completely saturated mode and exhibits a narrow PHD. On the other hand, I measured the PHDs and the spatial resolutions of the prototype detector with various potentials applied, and revealed the following points.

(1) The spatial resolution depends on the PHD, especially on the number of the events with low gains. This result is explained by the dependency of the resolution on the SNR of the output pulses.

(2) Applying the negative V_g reduces the width of the PHD from PHR=165% (V_g=0V) to 38% (V_g=-205V). This result is consistent with that of the calculation.

(3) Applying the negative V_g improves the spatial resolution by ~14%. This result is explained by the results of (1) and (2).

Finally, the spatial resolution of 54 μm, corresponding to 400×400 pixels in my detector, was achieved. I can optimize the technique using five MCPs and a RAE and apply it to the future missions. Further measurements, however, with a higher potential applied between the Z-stack output and the RAE are necessary to achieve a higher spatial resolution.

5 Concluding Remarks

The present study has confirmed that a remote sensing with EUV techniques is a promising means to explore the Earth's plasmasphere. The plasmasphere and its outer region are full of unsolved problems which are difficult to clarify by *in-situ* observations alone. Global EUV imaging enables us to shed new light to the physics of these regions. This thesis details the analysis on the plasmasphere images obtained by the EUV imager on the IMAGE satellite, the instrumentation and calibration of the UPI-TEX imager on the SELENE satellite, and the development of a high-resolution detector for future missions.

I statistically examined the plasmapause response to the southward turning of the IMF using sequential global images of the plasmasphere. The extreme ultraviolet (EUV) imager on the IMAGE satellite clearly observed inward motion of the plasmapause driven by the southward turning of the IMF. I surveyed the EUV data in the 2000–2001 period and found 16 events. Using the sequential EUV images, I have shown that the plasmapause response to the southward turning of the IMF takes 10–30 min, and average 18 min. It is consistent with the timescale derived from the ionospheric observations. Therefore the result indicates that the electric field penetrates from the magnetopause to the inner magnetosphere through the ionosphere. Chapter 2 deals with this topic.

The SELENE satellite was launched in 2007 and sent to the Moon. From the lunar orbit, the UPI-TEX will image the Earth's plasmasphere and the polar wind at O II (83.4 nm) and He II (30.4 nm) emissions. The instrumentation and calibration of the UPI-TEX imager has been presented in Chapter 3. The UPI-TEX imager has a total efficiency of 0.014 cps/Rayleigh/bin for the He II (30.4 nm) and 0.0036 cps/Rayleigh/bin for the O II (83.4 nm). For imaging the main body of the plasmasphere at He II (30.4 nm) emission, the UPI-TEX imager achieves the temporal resolution of 2 min and the spatial resolution of 0.09 R_E with a high reliability (SNR=3). Imaging of the plasmasphere will improve our understanding of the distribution of plasma in the inner magnetosphere and the forces that control it. In addition, the images will be useful for establishing the global context that can enhance the interpretation of *in-situ* measurements. On the other hand, the 30-min exposure with 0.5 R_E resolution allows us to image the polar wind by O II (83.4 nm) emission with SNR=2. The remote sensing at

O II by UPI-TEX will give the first global image of the polar wind and make significant contributions to our understanding of the transport routes and mechanisms of the cold O^+ ions.

In Chapter 4, I have presented the development of a high-resolution detector using five MCPs in a set of V- and Z-stacks and an RAE for the future missions. The effect of the negative potential applied across the inter-stack gap on the PHD and the spatial resolution has been investigated. As a result, the calculation with a simple ballistic model showed that the negative inter-stack potential reduced the size of the electron cloud by ~70%. The experiments furthermore revealed that applying the negative inter-stack potential reduced the width of the PHD by ~80% and improved the spatial resolution by ~14%. Finally, the spatial resolution of 54 μm, corresponding to 400×400 pixels in my detector, was achieved. Based on these results, I can optimize and apply this technique to the future missions.

Remaining Problems

In Chapter 2, using sequential EUV images of the plasmasphere I have shown that the plasmapause response to the southward turning of the IMF takes 10-30 min, with an average of 18 min. However, the result should be re-investigated using a more completed data set of EUV images because only 16 events were found in my search due to the limited EUV data. The IMAGE satellite orbits near the Earth, with the apogee of ~8 R_E. As such, it cannot always monitor the whole plasmasphere, and there is always an interval of at least several hours between images, which makes it difficult to estimate the time lag between the IMF arrival at the magnetosphere and plasmasphere evolution. In addition, a higher temporal resolution than that of the EUV instrument (10 min) is preferable to compare the plasmapause motion with the changes of the solar wind observed at the resolution of ~1 min.

The observation by the UPI-TEX imager improves the number of events because SELENE provides the best platform to command a panoramic view of the whole plasmasphere. I can re-investigate the plasmapause response to the solar wind using much more sequential images obtained by UPI-TEX. On the other hand, the temporal resolution is not effectively improved with respect to observing the plasmapause motion. The typical velocity of the plasmapause caused by the enhanced

convection is ~0.02 R_E/min, while the UPI-TEX imager has only a spatial resolution of 0.1 R_E. Therefore, the spatial resolution of 0.02 R_E, e.g. corresponding to 500×500 pixels in the field of view of 10 R_E, is required to distinguish the plasmapause motion at a temporal resolution of the order of ~1 min. I have developed a high-resolution detector using V- and Z-stack MCPs and an RAE and achieved a spatial resolution of 400×400 pixels, as described in Chapter 4. Further examination of the dependency of the spatial resolution on the potential applied between the Z-stack output and the RAE is necessary to achieve a higher spatial resolution.

Acknowledgements

The author wishes to express his sincere appreciation to Dr. I. Yoshikawa of the University of Tokyo for his guidance during the master's course and for stimulating discussions. The author would like to thank Dr. A. Yamazaki of Institute of Space and Astronautical Science for offering valuable suggestions and guidance throughout the present work as well as supporting the calibration of UPI-TEX. The author is grateful to Mr. K. Yoshioka for his continuing interest and encouragement. The author also thanks Dr. N. Iwagami, Professor M. Hoshino, Professor M. Hirahara, Dr. T. Yokoyama, and Professor M. Nakamura for providing important comments.

The author appreciates the help received from Ms. M. Hirai with analyzing the IMAGE EUV data. The authors would like to thank Dr. B. R Sandel for his assistance in the processing of EUV data available at http://euv.lpl.arizona.edu/euv/. The author also thanks Dr. N. Ness, Dr. C. Smith and the ACE science center for ACE MAG data and Dr. D. McComas for ACE SWEPAM data. The author is grateful to all of the members of the UPI team and the SELENE project team for their effort in achieving a successful mission.

The author also wishes to thank Dr. S. Kameda, Mr. J. Ono, Mr. F. Ezawa, Mr. T. Toyota, Mr. G. Ogawa, Dr. M. N. Nishino, Dr. S. Ohtsuki, and other members of Yoshikawa Lab, Iwagami Lab, and Nakamura Lab for their emotional assistance and friendship.

References

Abe, T., B. A. Whalen, A. W. Yau, R. E. Horita, S. Watanabe, and E. Sagawa (1993), EXOS D (Akebono) suprathermal mass spectrometer observations of the polar wind, *J. Geophys. Res.*, *98*, 11,191.

Abe, T., S. Watanabe, B. A. Whalen, A. W. Yau, and E. Sagawa (1996), Observations of polar wind and thermal ion outflow by Akebono/SMS, *J. Geomag. Geoelectr.*, *48*, 319.

Axford, W. I. (1968), The polar wind and the terrestrial helium budget, *J. Geophys. Res.*, *73*, 6,855.

Banks, P. M. and T. E. Holzer (1968), The polar wind, *J. Geophys. Res.*, *73*, 6846.

Banks, P. M., A. F. Nagy, and W. I. Axford (1971), Dynamical behavior of thermal protons in the mid-latitude ionosphere and magnetosphere, *Planet. Space Sci.*, *19*, 1,053.

Bronshteyn, I. M., A. V. Yevdokimov, V. M. Stozharov, and A. M. Tyutikov (1979), *Radio Eng. Electron. Phys.*, *24*, 150.

Burch, J. L., S. B. Mende, D. G. Mitchell, T. E. Moore, C. J. Pollock, B. W. Reinisch, B. R. Sandel, S. A. Fuselier, D. L. Gallagher, J. L. Green, J. D. Perez, and P. H. Reiff (2001a), Views of Earth's magnetosphere with the IMAGE satellite, *Science*, *291*(5504), 619.

Burch, J. L., D. G. Mitchell, B. R. Sandel, P. C. Brandt, and M. Wüest (2001b), Global dynamics of the plasmasphere and ring current during magnetic storms, *Geophys. Res. Lett.*, *28*(6), 1159.

Burton, R. K., R. L. McPherron, and C. T. Russell (1975), The terrestrial magnetosphere: A half-wave rectifier of the interplanetary electric field, *Science*, *189*, 717.

Carpenter, D. L. (1963), Whistler evidence of a 'knee' in the magnetospheric ionization density profile, *J. Geophys. Res.*, *68*, 1,675.

Carpenter, D. L., and J. Lemaire (1997), Erosion and recovery of the plasmasphere in the plasmapause region, *Space Sci. Rev.*, *80*, 153.

Chakrabarti, S. (1993), Magnetospheric Imagery and Atmospheric Remote Sensing, *Optic. Eng.*, *32*, 3007.

Chakrabarti, S., F. Paresce, S. Bowyer, Y. T. Chiu, and A. Aikin (1982), Plasmaspheric

helium ion distribution from satellite observations of He II 304 Å, *Geophys. Res. Lett.*, *9*, 151.

Chandler, M. O., J. H. Waite Jr., and T. E. Moore (1991), Observations of polar ion outflows, *J. Geophys. Res.*, *96*, 1,421.

Chappell, C. R. (1974), The convergence of fact and theory on magnetospheric convection, *Astrophys. Space Sci. Lib.*, *42*, 277.

Chappell, C. R., K. K. Harris, and G. W. Sharp (1970), A study of the influence of magnetic activity on the location of the plasmapause as measured by OGO 5, *J. Geophys. Res.*, *75*, 50.

Chappell, C. R., K. K. Harris, and G. W. Sharp (1971), The relationship of the plasmasphere and the stable auroral red arcs in the magnetic storm of October 29 to November 7, 1968, *Astrophys. Space Sci. Lib.*, *24*, 73.

Chen, A. J. and R. A. Wolf (1972), Effects on the plasmasphere of a time-varying convection electric field, *Planet. Space Sci.*, *20*, 483.

Chiu, Y. T., R. M. Robinson, G. R. Swenson, S. Chakrabarti, and D. S. Evans (1986), Imaging the outflow of ionospheric ions into the magnetosphere, *Nature*, *322*, 441.

Chiu, Y. T., R. M. Robinson, and H. L. Colin (1990), Magnetospheric and exospheric imaging in the extreme ultraviolet, *Geophys. Res. Lett.*, *17*, 267.

Cotton, D. M., R. Conant, and S. Chakrabarti (1993), Wide-angle geocoronal telescope: a He-II 304-Å plasmaspheric imager, *Optic. Eng.*, *32*, 3170, 1993.

Dungey, J. W. (1961), Interplanetary magnetic field and auroral zones, *Phys. Rev. Lett.*, *6*, 47.

Firmani, C., E. Ruiz, C. W. Carlson, M. Lampton, and F. Paresce (1982), High-resolution imaging with a two-dimensional resistive photon counter, *Rev. Sci. Instrum.*, *53*(5), 570.

Floryan, R. F., and C. B. Johnson (1989), Resistive anode photomultiplier tube optimum operating conditions for photon correlation experiments, *Rev. Sci. Instrum.*, *60*(3), 339.

Fuselier, S. A., A. G. Ghielmetti, T. E. Moore, M. R. Collier, J. M. Quinn, G. R. Wilson, P. Wurz, S. B. Mende, H. U. Frey, C. Jamar, J.-C. Gerard, and J. L. Burch (2001), Ion outflow observed by IMAGE: Implications for source regions and heating mechanisms, *Geophys. Res. Lett.*, *28*, 1,163.

Goldstein, J., M. Spasojević, P. H. Reiff, B. R. Sandel, W. T. Forrester, S. L. Gallagher,

and B. W. Reinisch (2003a), Identifying the plasmapause in IMAGE EUV data using IMAGE RPI in situ steep density gradients, *J. Geophys. Res.*, *108*(A4), 1147, doi:10.1029/2002JA009475.

Goldstein, J., B. R. Sandel, W. T. Forrester, and P. H. Reiff (2003b), IMF-driven plasmasphere erosion of 10 July 2000, *Geophys. Res. Lett.*, *30*(3), 1146, doi:10.1029/2002GL016478.

Goldstein, J., B. R. Sandel, P. H. Reiff, and M. R. Hairston (2003c), Control of plasmaspheric dynamics by both convection and sub-auroral polarization stream, *Geophys. Res. Lett.*, *30*(24), 2243, doi:10.1029/2003GL018390.

Goldstein, J., B. R. Sandel, M. F. Thomsen, M. Spasojevic´, and P. H. Reiff (2004a), Simultaneous remote-sensing and in situ observations of plasmaspheric drainage plumes, *J. Geophys. Res.*, 109, A03202, doi:10.1029/2003JA010281.

Goldstein, J., R. A. Wolf, B. R. Sandel, and P. H. Reiff (2004b), Electric fields deduced from plasmapause motion in IMAGE EUV images, *Geophys. Res. Lett.*, 31(1), L01801, doi:10.1029/2003GL018797.

Goldstein, J., B. R. Sandel, W. T. Forrester, M. F. Thomsen, and M. R. Hairston (2005), Global plasmasphere evolution 22–23 April 2001, *J. Geophys. Res.*, 110, A12218, doi:10.1029/2005JA011282.

Grebowsky, J. M. (1971), Time Dependent plasmapause motion, *J. Geophys. Res*, *75*, 4,329.

Hairston, M. R., and R. A. Heelis (1995), Response time of the polar ionospheric convection pattern to changes in the north-south direction of the IMF, *Geophys. Res. Lett.*, *22*, 631.

Hashimoto, K. K., T. Kikuchi, and Y. Ebihara (2002), Response of the magnetospheric convection to sudden interplanetary magnetic field changes as deduced from the evolution of partial ring currents, *J. Geophys. Res.*, *107*(A11), 1337, doi:10.1029/2001JA009228.

Johnson, C. Y., J. M. Young, and J. C. Holmes (1971), Magnetoglow-A new geophysical resource, *Science*, *171*, 379.

Kikuchi, T., H. Lűhr, T. Kitamura, O. Saka, and K. Schlegel (1996), Direct penetration of the polar electric field to the equator during a DP2 event as detected by the auroral and equatorial magnetometer chains and the EISCAT radar, *J. Geophys. Res.*, *101*, 17,161.

Lampton, M., and C. W. Carlson (1979), Low-distortion resistive anodes for two-dimensional position-sensitive MCP systems, *Rev. Sci. Instrum.*, *50*(9), 1,093.

Lemaire, J. (1974), The 'Roche-limit' of ionospheric plasma and the formation of the plasmapause, *Planet. Space Sci.*, *22*, 757.

Lemaire, J. (1985), Frontiers of the Plasmasphere (Theoretical Aspects), Universite´ Catholique de Louvain, Faculte´ des Sciences, Louvain-la-Neuve, ISBN 2-87077-310-2.

Lemaire, J. F., and K. I. Gringauz (1998), The Earth's plasmasphere, Cambridge Univ. Press, New York.

Lu, G., T. E. Holzer, D. Lummerzheim, J. M. Ruohoniemi, P. Stauning, O. Troshichev, P. T. Newell, M. Brittnacher, and G. Parks (2002), Ionospheric response to the interplanetary magnetic field southward turning: Fast onset and slow reconfiguration, *J. Geophys. Res.*, *107*(A8), 1153, doi:10.1029/2001JA000324.

Martin, C., and S. Bowyer (1982), Quantum efficiency of opaque CsI photocathodes with channel electron multiplier arrays in the extreme and far ultraviolet, *Appl. Opt.*, *21*, 4,206.

Matsui, H., T. Mukai, S. Ohtani, K. Hayashi, R. C. Elphic, M. F. Thomsen, and H. Matsumoto (1999), Cold dense plasma in the outer magnetosphere, *J. Geophys. Res.*, *104*, 25,077.

McComas, D. J., S. J. Bame, P. Barker, W. C. Feldman, J. L. Phillips, P. Riley, and J. W. Griffee (1998), Solar Wind Electron Proton Alpha Monitor (SWEPAM) for the Advanced Composition Explorer, *Space Sci. Rev.*, *86*, 563.

Meier, R. R. (1991), Ultraviolet spectroscopy and remote sensing of the upper atmosphere, *Space Sci. Rev.*, *58*, 1.

Meier, R. R. and C. S.Weller (1972), EUV resonance radiation from helium atoms and ions in the geocorona, *J. Geophys. Res.*, *77*, 1,190.

Meier, R. R., A. C. Nicholas, J. M. Picone, D. J. Melenez-Alvira, G. I. Ganguli, M. A. Reynolds, and E. C. Roelof (1998), Inversion of plasmaspheric EUV remote sensing data from the STP 72-1 satellite, *J. Geophys. Res.*, *103*, 17,505.

Moldwin, M. B., M. F. Thomsen, S. J. Bame, D. J. McComas, and K. R. Moore (1994), An examination of the structure and dynamics of the outer plasmasphere using multiple geosynchronous satellites, *J. Geophys. Res.*, *99*, 11,475.

Moore, T. E., D. J. Chornay, M. R. Collier, F. A. Herrero, J. Johnson, M. A. Johnson, J.

W. Keller, J. F. Laudadio, J. F. Lobell, K. W. Ogilvie, P. Rozmarynowski, S. A. Fuselier, A. G. Ghielmetti, E. Hertzberg, D. C. Hamilton, R. Lundgren, P. Wilson, P. Walpole, T. M. Stephen, B. L. Peko, B. Van Zyl, P. Wurz, J. M. Quinn, and G. R. Wilson (2000), The low energy neutral atom imager for IMAGE, *Space Sci. Rev.*, *91*, 155.

Moore, T. E., M. R. Collier, J. L. Burch, D. J. Chornay, S. A. Fuselier, A. G. Ghielmetti, B. L. Giles, D. C. Hamilton, F. A. Herrero, J. W. Keller, K. W. Ogilvie, B. L. Peko, J. M. Quinn, T. M. Stephen, G. R. Wilson, and P.Wurz (2001), Low energy neutral atoms in the magnetosphere, *Geophys. Res. Lett.*, *28*, 1,143.

Murakami, G., K. Yoshioka, and I. Yoshikawa (2006), Development of Mg/SiC multilayer mirrors, *Proc. SPIE*, *6317*, 631714-1.

Murakami, G., M. Hirai, and I. Yoshikawa (2007), The plasmapause response to the southward turning of the IMF derived from sequential EUV images, *J. Geophys. Res.*, *112*, A06217, doi:10.1029/2006JA012174.

Murayama, T. (1982), Coupling function between solar wind parameters and geomagnetic indices, *Rev. Geophys. Space Phys.*, *20*, 623.

Nakamura, M., I. Yoshikawa, A. Yamazaki, K. Shiomi, Y. Takizawa, M. Hirahara, K. Yamashita, Y. Saito, and W. Miyake (2000), Terrestrial plasmaspheric imaging by an extreme ultraviolet scanner on Planet-B, *Geophys. Res. Lett.*, *27*(2), 141.

Nishida, A. (1966), Formation of plasmapause, or magnetospheric plasma knee, by the combined action of magnetospheric convection and plasma escape from the tail, *J. Geophys. Res.*, *71*, 5,669.

Ogawa, T., and T. Tohmatsu (1971), Sounding rocket observation of helium 304- and 584-Å glow, *J. Geophys. Res.*, *76*, 6136.

Paresce, F., C. S. Bowyer, and S. Kumar (1974), On the distribution of He^+ in the plasmasphere from observations of resonantly scattered He II 304 Å radiation, *J. Geophys. Res.*, *79*, 174.

Park, C. G. (1970), Whistler observations of the interchange of ionization between the ionosphere and the protonosphere, *J. Geophys. Res.*, *75*, 4,249.

Pierrard, V., and J. Cabrera (2005), Comparisons between EUV/IMAGE observations and numerical simulations of the plasmapause formation, *Ann. Geophys.*, *23*, 2635.

Pierrard, V., and J. Cabrera (2006), Dynamical simulations of plasmapause

deformations, *Space Sci. Rev.*, *122*, 119.

Rairden, R. L., L. A. Frank, and J. D. Craven (1986), Geocoronal imaging with Dynamics Explorer, *J. Geophys. Res.*, *91*, 13,613.

Ridley, A. J., G. Lu, C. R. Clauer, and V. O. Papitashvili (1998), A statistical study of the ionospheric convection response to changing interplanetary magnetic field conditions using the assimilative mapping of ionospheric electrodynamics technique, *J. Geophys. Res.*, *103*(A3), 4023.

Roelof, E. C., B. H. Mauk, Barry, and R. R. Meier (1992), Instrument requirements for imaging the magnetosphere in extreme ultraviolet and energetic neutral atoms derived from computer-simulated images, *Proc. SPIE*, *1744*, 19.

Roelof, E. C., and A. J. Skinner (2000), Extraction of ion distributions from magnetospheric ENA and EUV images, *Space Sci. Rev.*, *91*, 437.

Ruohoniemi, J. M., and R. A. Greenwald (1998), The response of highlatitude convection to a sudden southward IMF turning, *Geophys. Res. Lett.*, *25*, 2913.

Saito, M., Y. Saito, K. Asamura, and T. Mukai (2007), Spatial charge cloud size of microchannel plates, *Rev. Sci. Instrum.*, *78*, 023302.

Sandel, B. R., A. L. Broadfoot, C. C. Curtis, R. A. King, T. C. Stone, R. H. Hill, J. Chen, O. H. W. Siegmund, R. Raffanti, D. D. Allred, R. S. Turley, and D. L. Gallagher (2000), The Extreme Ultraviolet Imager investigation for the IMAGE mission, *Space Sci. Rev.*, *91*, 197.

Sandel, B. R., R. A. King, W. T. Forrester, D. L. Gallagher, A. L. Broadfoot, and C. C. Curtis (2001), Initial results from the IMAGE Extreme Ultraviolet Imager, *Geophys. Res. Lett.*, *28*, 1,439.

Sandel, B. R., J. Goldstein, D. L. Gallagher, and M. Spasojević (2003), Extreme Ultraviolet Imager observations of the structure and dynamics of the plasmasphere, *Space Sci. Rev.*, *109*, 25.

Schulz, M. and H. C. Koons (1972), Thermalization of colliding ion streams beyond the plasmapause, *J. Geophys. Res.*, *77*, 248.

Seki, K., M. Hirahara, T. Terasawa, I. Shinohara, T. Mukai, Y. Saito, S. Machida, and T. Yamamoto (1996), Coexistence of Earth-origin O^+ and solar wind-origin H^+/He^{++} in the distant magnetotail, *Geophys. Res. Lett.*, *23*, 985.

Seki, K., M. Hirahara, T. Terasawa, T. Mukai, and S. Kokubun (1999), Properties of He^+ beams observed by Geotail in the lobe/mantle regions: Comparison with O^+ beams,

J. Geophys. Res., *104*, 6,973.

Seki, K., R. C. Elphic, M. Hirahara, T. Terasawa, and T. Mukai (2001), On atmospheric loss of oxygen ions from earth through magnetospheric processes, *Science*, *291*, 1,939.

Seki, K., M. Hirahara, T. Terasawa, T. Mukai, and R. Elphic (2002), Dynamics of oxygen ions in the Earth s magnetotail: Geotail and FAST observations, *34th COSPAR Scientific Assembly*, 2002.

Siegmund, O. H. W., J. Vallerga, and B. Wargelin (1988), Background events in microchannel plates, *IEEE Trans. Nucl. Sci.*, *35*(1), 524.

Smith, C. W., J. L'Heureux, N. F. Ness, M. H. Acuna, L. F. Burlaga, and J. Scheifele (1998), The ACE magnetic fields experiment, *Space Sci. Rev.*, *86*, 613.

Spasojević, M., J. Goldstein, D. L. Carpenter, U. S. Inan, B. R. Sandel, M. B. Moldwin, and B. W. Reinisch (2003), Global response of the plasmasphere to a geomagnetic disturbance, *J. Geophys. Res.*, *108*(A9), 1340, doi:10.1029/2003JA009987.

Timothy, J. G., and R. L. Bybee (1975), One-dimensional photon-counting detector array for use at EUV and soft X-ray wavelngths, *Appl. Opt.*, *41*, 1,632.

Tournianski, M. R., P. G. Carolan, and R. J. Akers (2004), Enhanced microchannel plate performance at high particle fluxes by pulsed exposure mode of operation, *Rev. Sci. Instrum.*, *75*(9), 2854.

Tremsin, A. S., and O. H. Siegmund (1999), Spatial distribution of electron cloud footprints from microchannel plates: Measurements and modeling, *Rev. Sci. Instrum.*, *70*(8), 3,282.

Weller, C. S., and R. R. Meier (1974), First satellite observations of the He^+ 304-Å radiation and its interpretation, *J. Geophys. Res.*, *79*, 1,572.

Williams, D. J., E. C. Roelof, and D. G. Mitchell (1992), Global magnetospheric imaging, *Rev. Geophys.*, *30*, 183.

Wilson, G. R., J. L. Horwitz, and J. Lin (1992), A semikinetic model for early stage plasmasphere refilling. I - Effects of Coulomb collisions, *J. Geophys. Res.*, *97*, 1,109.

Wiza, J. L., P. R. Henkel, and R. L. Roy (1977), Improved microchannel plate performance with a resistive anode encoder, *Rev. Sci. Instrum.*, *48*(9), 1,217.

Yamazaki, A., S. Tashiro, Y. Nakasaka, I. Yoshikawa, W. Miyake, and M. Nakamura (2002), Sounding-rocket observation of O II 83.4-nm emission over the polar

ionosphere, *Geophys. Res. Lett.*, 29, 2,005.

Yamazaki, A., I. Yoshikawa, K. Shiomi, Y. Takizawa, W. Miyake, and M. Nakamura (2006), Latitudinal variation of the solar He I 58.4 nm irradiance from the optical observation of the interplanetary He I emission, *J. Geophys. Res.*, *111*(A6), CiteID A06106.

Yoshikawa, I., M. Nakamura, M. Hirahara, Y. Takizawa, K. Yamashita, H. Kunieda, T. Yamazaki, K. Misaki, and A. Yamaguchi (1997), Observation of He II emission from the plasmasphere by a newly developed EUV telescope on board sounding rocket S-520-19, *J. Geophys. Res.*, *76*, 19,897.

Yoshikawa, I., A. Yamazaki, K. Shiomi, M. Nakamura, K. Yamashita, and Y. Takizawa (2000a), Evolution of the outer plasmasphere during low geomagnetic activity observed by the EUV scanner onboard Planet-B, *J. Geophys. Res.*, *105*(A12), 27,777.

Yoshikawa, I., A. Yamazaki, K. Shiomi, K. Yamashita, Y. Takizawa, and M. Nakamura (2000b), Photometric measurement of cold helium ions in the magnetotail by an EUV scanner onboard Planet-B: Evidence of the existence of cold plasmas in the near-Earth plasma sheet, *Geophys. Res. Lett.*, *27*(21), 3657.

Yoshikawa, I., A. Yamazaki, K. Shiomi, K. Yamashita, Y. Takizawa, and M. Nakamura (2001), Interpretation of the He II (304 Å) EUV image of the inner magnetosphere by using empirical models, *J. Geophys. Res.*, *106*(A11), 25,745.

Yoshikawa, I., T. Murachi, H. Takenaka, and S. Ichimaru (2005), Multilayer coating for 30.4 nm, *Rev. Sci. Instrum.*, *76*, Issue 6, 066109.

Yoshikawa, I., A. Yamazaki, G. Murakami, K. Yoshioka, S. Kameda, F. Ezawa, T. Toyota, W. Miyake, M. Taguchi, M. Kikuchi, M. Nakamura, T. Sakanoi, and S. Okano (2008), Telescope of extreme ultraviolet (TEX) onboard SELENE: science from the Moon, *Earth, Planets and Space*, in press.

Zanodvorov, N. P., N. K. Zolina, A. M. Tyutikov, and Y. A. Flegontov (1980), Estimation of the modulation-transfer functions of microchannel plates, *Radio Eng. Electron. Phys.*, *25*, 129.